STRUCTURE, MINERALOGY, VITRINITE REFLECTANCE, AND SHEAR HEATING OF THE 3067 M MD FAULT FROM SAFOD: AN INVESTIGATION OF OFF-FAULT FRICTIONAL HEATING

A Thesis

by

JONATHAN R. FRY

Submitted to the Office of Graduate and Professional Studies of
Texas A&M University
in partial fulfillment of the requirements for the degree of

MASTER OF SCIENCE

Chair of Committee,	Judith S. Chester
Committee Members,	Frederick M. Chester
	Luciana R. Barroso
Head of Department,	Julie Newman

May 2020

Major Subject: Geology

ABSTRACT

This study focuses on the 3067 m MD fault captured in core recovered from the western damage zone of the San Andreas fault during Phase 1 drilling of the San Andreas Fault Observatory at Depth (SAFOD) before the borehole intersected the main trace of the San Andreas fault near Parkfield, California. The main goal of this study was to determine if there was evidence of slip-induced frictional heating using vitrinite reflectance geothermometry of organic material in the host rock and shear zone. The 3067 m MD fault juxtaposes a siltstone and an arkosic sandstone across the shear zone that displays inhomogeneous deformation. The host lithologies and shear zone were described according to their elemental and mineralogical composition.. Numerical modeling of frictional heating from fault slip constrained possible orientations of the fault during slip, maximum temperature within the shear zone and host rock during and after slip, and expected vitrinite reflectance response of organic particles following slip magnitudes of 0.01 to 0.05 m. Four distinct structural units were identified within the shear zone and characterized by a reduction in grain size, development of shear textures, and an increase in clay and indistinguishable phases. The 3067 m MD fault displays localization of slip and comminution, consistent with, but not unique to seismic slip. The fault rock also contains evidence of physical and mineralogical alteration associated with faulting. Vitrinite reflectance values across the 3067 m MD fault average ~1.7% Ro compared to the modeled maximum predicted reflectance of 1.3% Ro due to burial, consistent with faults showing large cumulative slip. Numerical modeling of stress orientation suggests a sub-vertical fault orientation and coefficient of sliding friction of 0.4. At these conditions

observed reflectance values are explained by a slip magnitude of 0.03 m on a 0. 5 mm thick shear zone producing a maximum temperature of ~1000 °C. The high-vitrinite-reflectance particles could reflect some localized seismic heating.

ACKNOWLEDGEMENTS

I am tremendously grateful to the Texas A&M University Department of Geology and Geophysics for their enduring commitment to developing students into scientists. Specifically, I would like to thank Judi Chester and Fred Chester for their patience and support of this work. Thank you as well to all of the faculty and students of the Center for Tectonophysics for immeasurable academic, professional, and personal enrichment for which I will always be thankful.

CONTRIBUTORS AND FUNDING SOURCES

Contributors

This work was supported by a thesis committee consisting of Professors Judith S. Chester and Frederick M. Chester of the Department of Geology and Geophysics and Professor Luciana R. Barroso of the Department of Civil and Environmental Engineering.

The X-ray fluorescence data from Chapter 3 were collected with support of Professor Michael M. Tice. The SEM images in Chapter 3 were collected with the support of Tom Stephens of the Microscopy and Imaging Center. The collection and analysis of elemental data in Chapter 3 were supported by Dr. Ray Guillemette. The vitirinite reflectance data were collected with the support of Drs. Hamed Sanei and Omid Ardakani of the Canadian Geological Survey.

All other work conducted for the thesis was completed by the student independently.

Funding Sources

Graduate study was supported by fellowships from the Texas A&M University College of Geosciences, the Department of Geology and Geophysics, and the Center for Tectonophysics. This research was also supported by a Geological Society of America Graduate Student Research Grant, the AAPG Foundation James E. Hooks Memorial Grant, and by the NSF-EarthScope grants EAR-0454525 and EAR-0643339 to J. Chester and F. Chester.

TABLE OF CONTENTS

LIST OF FIGURES

FIGURE Page

LIST OF TABLES

TABLE Page

1. INTRODUCTION

The energy released during an earthquake is partitioned into three components, radiated energy, E_R, off-fault fracture energy and thermal energy, E_G, and thermal energy from frictional sliding, $E_{N.}$ (Kanamori & Rivera, 2006) The manner and mechanisms of the partitioning and release of energy is a topic of ongoing work with implications for hazard assessment and the understanding of fundamental geomechanical fault processes. Analyses of structures in fault cores and their associated damage zones suggest that while jointing and Mode I microcracking account for only a few percent of the total energy budget (Chester et al., 2005), off-fault frictional sliding on subsidiary faults may contribute a significant source of the heat described by E_G (Chester & Chester, 2006; Ben-Zion & Sammis, 2013). This may be especially true in regions of complex fault geometry where the damage zone of a fault core displays a high density of off-fault damage (Ben-Zion & Sammis, 2013). Gaining a better understanding of the role of processes described by E_G is critical to accurately partitioning the potential energy and to our overall understanding of the energetics of earthquake rupture.

The 3067 m measured depth (MD) fault is the largest subsidiary fault captured in the western damage zone during the second coring stage of Phase 1 drilling at the San Andreas Fault Observatory at Depth (SAFOD) (Figure 1; Schulz & Wallace, 2016). The 3067 m MD fault was encountered at ~2.5 km true depth, and is about 300 m west of the Southwest Deforming Zone (SDZ), the western most actively creeping trace of the SAF at SAFOD (Almeida et al., 2005; Zoback et al., 2011). The 3067 m MD fault is bounded

by the active SDZ to the east and the Buzzard Canyon Fault (Springer et al., 2009) to the west.

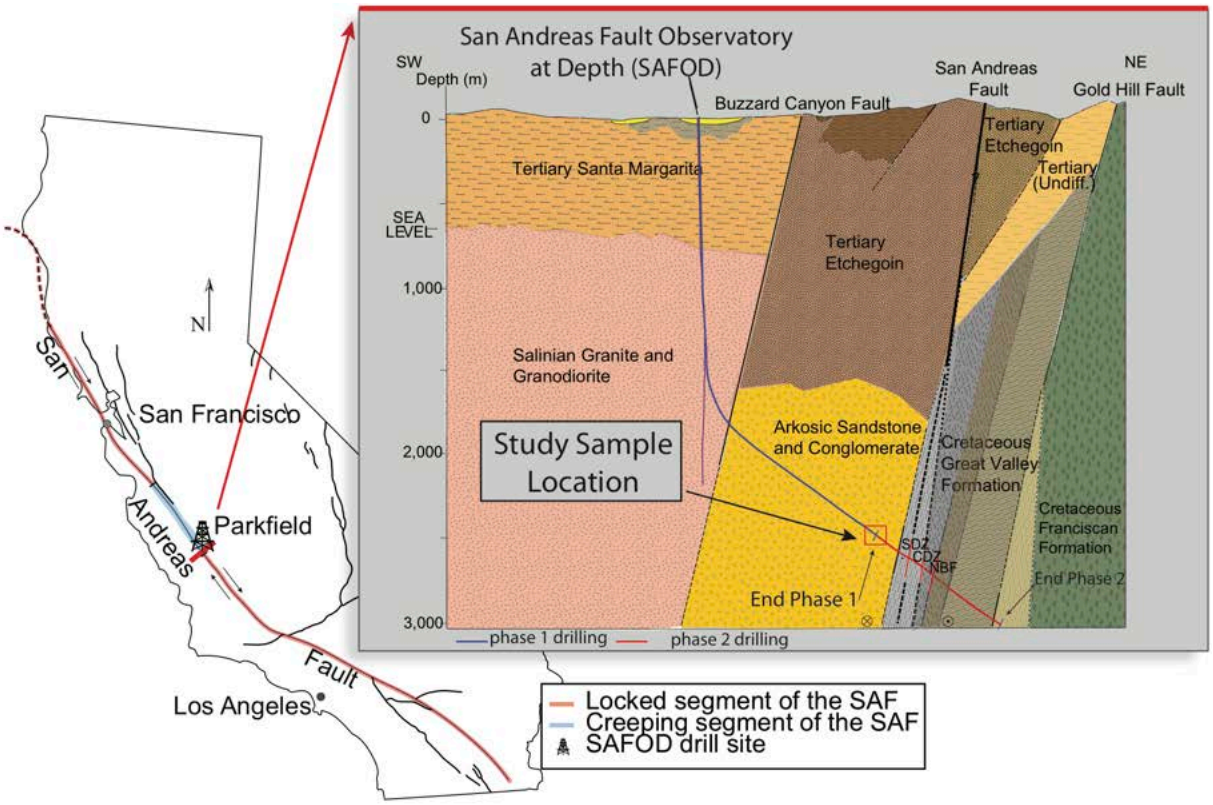

Figure 1: Location Map and Cross Section of the SAFOD Borehole. Location map (left) and cross section (right) showing the SAFOD borehole crossing the San Andreas fault near Parkfield, CA. The borehole and cross section are approximately perpendicular to the fault trace. Map modified from Schulz & Wallace (2016, http://pubs.usgs.gov/gip/earthq3/where.html). Cross section shows rock units cut by the borehole during Phase 1 and 2 drilling, modified from Zoback et al. (2010 & 2011).

The block cut by the 3067 m MD fault has been transported about 315 km northwest by right-lateral movement along the SAF system (Graham et al., 1989).

The SAFOD samples collected from the SAFOD scientific borehole provide the opportunity to describe and study subsidiary faults cutting the damage zone of a major plate boundary fault at in-situ conditions, unaltered by exhumation, weathering, and other near-surface processes. The 3067 m MD fault, in particular, is significant in that it is the largest subsidiary fault cutting the western damage zone of the SAF that was captured by coring. A primary goal of this study is to determine if the 3067 m MD fault displays evidence of shear heating to test the hypothesis that repeated slip on this fault contributed to the E_G term. This study uses analytical electron beam microscopy, X-ray beam techniques, reflected light microscopy, and vitrinite reflectance analysis to describe the mineralogy and thermal history of the host rock and fault rock of the 3067 m fault. Numerical modeling of fault-slip-induced shear heating and vitrinite reflectance response is compared to observed vitrinite reflectance values to evaluate the mechanisms capable of producing observed values.

2. BACKGROUND

2.1 Frictional Heating from Fault Movement

Frictional heat generated by seismic slip is thought to be the greatest component of the earthquake energy budget (Kanamori & Rivera, 2006). The magnitude of frictional heating depends on several factors including fault strength, displacement rate, and slip localization. In general these factors are not well defined.

Sibson (2003) describes the magnitude of frictional heat, Q, generated by fault movement as a function of the shear strength of the fault, τ, and the slip distance, u (Sibson, 2003). Assuming constant shear strength and displacement, frictional heat is expressed as,

$$Q = \tau_f \cdot u \ (J/m^2) \quad (1)$$

The strength of a fault, τ_f, can be described as the product of the coefficient of sliding friction, μ, and the normal stress, σ_n. The coefficient of sliding can be considered a material property and is on the order of 0.6-0.7 for most silicate rocks (Byerlee, 1978). Estimates of fault strength, however, vary depending on assumptions made about the pore pressure and communication of fluids across the shear zone (Lachenbruch, 1980). As such, the effective stress, σ_{eff}, which is equal to the σ_n minus the pore pressure, is more properly used to describe the strength of faults.

The maximum temperature change, ΔT, from frictional heat generation in a shear zone depends on several factors including the τ_f, width of the shear, t_s, specific heat capacity, C_p, and density, ρ, of the rock, assuming no loss of heat from the shear zone (Sibson, 2003).

$$\Delta T = \frac{\tau_f u}{C_p \rho t_s} \quad (2)$$

This relationship can be used to determine mechanical properties of faults and characteristics of fault ruptures if the variables are known. The τ_f depends on μ, which is readily measured under quasi-static conditions; however, values of μ during seismic slip are uncertain due to the influence of dynamic weakening processes (e.g. Rice, 2006; Kitajima et al., 2011; Tullis, 2015). If dynamic weakening occurs during an earthquake, frictional heating can be greatly reduced, further complicating the ability to define the magnitude of E_N.

Sibson (2003) analyzed a range of slip displacements, fault strengths, and shear zone widths (Figure 2) and illustrated that relatively small magnitudes of displacement across very thin zones of shear are capable of producing melt (Sibson, 1975; 2003). In addition, because diagenetic and fluid-rock processes can be temperature dependent (Merriman, 1987), spikes in temperature generated during high-speed slip can drive mineral alteration reactions in host rocks adjacent to the shear zone.

Pseudotachylites are the only known features that provide unequivocal evidence of heating and localized slip at seismic velocities (Cowan, 1999; Sibson, 1975; Spray, 1997). Pseudotachylites are cohesive fine-grained or glassy fault rocks that often contain fragments of the wall rock. These rocks can only form at seismic slip rates when local temperatures increase enough to induce melting.

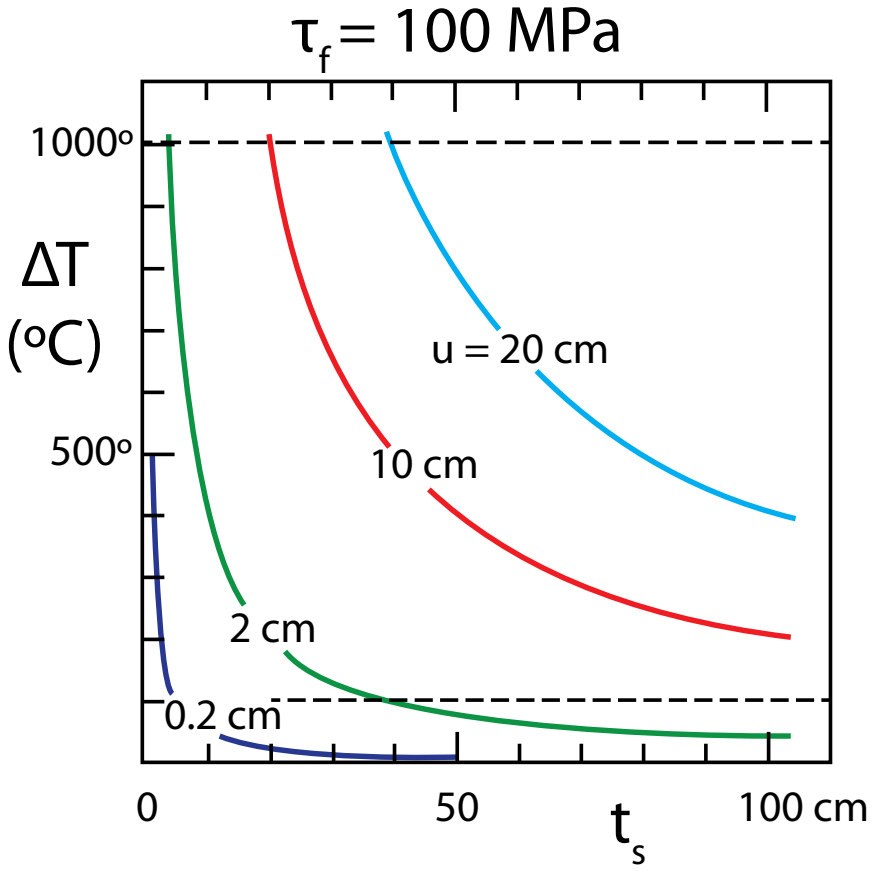

Figure 2: Adiabatic Temperature Rise from Faulting. Plot of temperature versus shear zone thickness t_s as a function of slip magnitude modified from Sibson (2003). Temperature rise assumes adiabatic heating within a 1 dimensional shear zone of thickness, t_s. Temperatures are calculated from equation 2 using values for specific heat, C_p, of 1000 J/kg °C, density, ρ, of 2500 kg/m^3, and a slip rate of 1 m s^{-1}.

2.2 Previous Work on the 3067 m MD Fault at SAFOD

The 3067 m MD fault is the largest subsidiary fault captured during the second coring stage of Phase 1 drilling at SAFOD. The mineralogy, basic microstructures, and frictional behavior of the fault rocks from the main structural domains of the fault have been discussed by previous studies (Kitajima et al., 2013; Schleicher et al., 2006; 2008; Solum et al., 2006; Tembe et al., 2006). Most of the existing work does not specify the exact sample locations or fault rock types studied from this fault, and therefore report bulk values for the entire zone. Kitajima et al., (2006) however, defined four main fault-rock units within the 3067 m MD fault, and provided X-ray diffraction (XRD) data for each unit. The fault-rock samples were analyzed in air-dried, glycolated and heated conditions (H. Kitajima, personal communication, 2012). Analysis of XRD patterns reveal that the units are similar in mineralogy to published, bulk data (Solum et al., 2006; Schleicher et al., 2009) but that the relative percent of clay phases varies by up to ~20% across the units analyzed. Samples showing polished surfaces and slickenlines with fibrous surfaces were identified in drill cuttings and on fragments taken from the core (Schleicher et al., 2006). Much of the work on this fault zone has focused on identifying the clay mineralogy as well as the microstructures of clays and fracture surfaces (Moore & Rymer, 2007; Schleicher et al., 2009; 2010; Tembe et al., 2006), because of the suspected link between a weak, creeping SAF and low-shear-strength clay minerals such as montmorillonite (Moore & Rymer, 2007).

Bulk mineralogical analysis revealed a clay-rich composition of 48-51% illite, 14-18% interlayered illite-smectite (I-S), 19-22% feldspar (plagioclase and potassium

feldspar), 11-17% quartz, and 1% chlorite (Solum et al., 2006; Tembe et al., 2006). Diagenetic models of the smectite to illite transition were used to understand the thermal history of the fault, and suggest a maximum burial temperature of ~170 °C (Schleicher et al., 2009). Detrital zircon fission track analyses on samples from the upper portion of the core from Phase 2 drilling (Figure 1) at 3122 – 3160 m MD suggest a maximum burial temperature less than 200 - 240 °C (Springer et al., 2009).

Interlayered I-S was found coating fracture surfaces and is interpreted as an explanation for the development of a weak fault due to the low shear strength of I-S (μ = ~0.2-0.3) (Schleicher et al., 2010). Some of the clay phases within the fault zone, including those found coating fracture surfaces, are thought to be neo-formed authigenic clays rather than detrital in origin (Schleicher et al., 2009; 2010). The authigenic origin is suggested by the existence of two polytypes of illite and I-S ($1M/1M_d$ and $2M_1$), one interpreted as the detrital fraction ($2M_1$) and the other the authigenic fraction ($1M/1M_d$). Argon age dating supports this interpretation with ages of formation for the youngest phases of 8.0 Ma ± 1.3 Ma, and 77 Ma ± 20 Ma for the older, detrital phases (Schleicher et al., 2010).

Low-speed (Tembe et al., 2006) and high-speed (Kitajima et al., 2006) friction experiments using samples from the 3067 m MD fault characterize the frictional strength properties of the fault. In low-speed friction experiments (0.01 – 1.0 m s^{-1}) Tembe et al. (2006) found evidence of low (0.4 – 0.55) quasi-static friction interpreted to be the result of high phyllosilicate content within the gouge. Kitajima et al. (2006) deformed samples from the four distinct fault rock units at coseismic slip rates of 1.3 m s^{-1} and found

consistent slip-strengthening followed by slip-weakening behavior with a lower steady-state coefficient of sliding friction of ~0.2 after slip distances of 5 - 10 m. This low coefficient of friction is consistent with the hypothesis that dynamic weakening mechanisms inhibit large heating events during localized coseismic slip on faults (Rice, 2006). Data suggest that extremely weak minerals (e.g. Moore & Rymer, 2007) or some degree of fault maturity and localization of slip (e.g. Chester & Chester, 1998) are necessary for low fault strength. Small displacement damage-zone faults, however, are expected to have normal coefficients of friction consistent with Byerlee's relation (Byerlee, 1978) and therefore could contribute to the E_G term (Ben-Zion & Sammis, 2013; Chester & Chester, 2006; Kanamori & Rivera, 2006).

3. STRUCTURE AND MINERALOGY OF THE 3067 M MD FAULT

3.1 Mineralogy and Alteration of the 3067 m MD Fault

3.1.1 Mineralogy and Alteration Background

Products of diagenetic and very-low-grade metamorphic reactions are found in the arkosic sandstone and siltstone units of the western damage zone captured during coring (Heron, 2011; Schleicher et al., 2009; Solum et al., 2006). Alteration reactions are often temperature (depth) dependent and their products can be used to interpret burial history (Frey, 1987). Alteration reactions in brittle fault zones are often facilitated by tensile and shear fractures that cut the damage zones, as the newly created fracture networks increase fluid circulation and mixing of fluids from different sources. These processes facilitate reaction kinetics, dissolution, advective mass transfer, and precipitation processes throughout the earthquake cycle. Formation of authigenic clay phases during and after shearing events changes the fluid-flow and mechanical properties of faults (Chester et al., 1993; Evans & Chester, 1995; Schleicher et al., 2009; Wibberley & Shimamoto, 2003). Relative differences in fault and host rock chemistry have been used to identify zones of enhanced fluid-rock interaction, mass transfer, and extrinsic conditions of deformation, and also to infer the strength of the fault (Evans & Chester, 1995; Grant, 2005; Schleicher et al., 2009).

Diagenetic and stress enhanced processes have been observed in the SAFOD core collected during Phase 1 drilling in the vicinity of the 3067 m MD fault (Schleicher et al., 2009). These include precipitation of laumontite, illite and illite-smectite, and other clay phases from the albitization and dissolution of feldspar, all of which are interpreted

to have been enhanced by stress at grain contacts (Heron, 2011; Schleicher et al., 2009; Solum et al., 2006; Springer et al., 2009). Identification of the type and distribution of alteration products within the 3067 m MD fault will help define zones of fluid compartmentalization, possible syn-deformation reactions, and diagenetic history.

The studies by Heron (2011) on incipient and small subsidiary faults within the arkosic sandstones from the SAFOD borehole quantified particle size development and mineralogical alteration as a function of mineralogy and strain. Many of the same analytical methods are used in this study and the work of Heron (2011) provides a reference for degree of alteration and deformation in nearby faults with similar lithology, but with less displacement.

The 3067 m MD fault was originally thought to be the western-most active trace of the San Andreas Fault due to its size and location at the eastern extent of the deviated borehole (J. Chester, personal communication, 2014). The fault rock was recovered in the core catcher detached from the upper core making in-situ orientation of the 3067 m MD fault difficult to determine. Almeida et al. (2005, 2007) and Almeida (2007) used the orientation of the fault with respect to the well bore axis to determine possible original orientations of the 3067 m MD fault. Other fractures within the intact core and fault rock surrounding the 3067 m MD fault were mapped and correlated to dominant fracture sets shallower in the core and in borehole image logs to further constrain the range of possible in-situ orientations.

3.1.2 Mineralogy and Alteration Methods

High-resolution images and elemental composition data from X-ray and electron beam instruments were collected to determine the alteration products within the 3067 m MD fault. Analytical methods for the determination of mineralogy follow in style of Heron (2011) in order to directly compare results from this study to those from Heron (2011).

The 3067 m MD fault sample was cut into 6 blocks that were polished and carbon-coated for electron beam microscopy (Figure 3). Quantitative compositional analyses and high-resolution imaging were performed on blocks 3067_3 and 3067_6 of the 3067 m MD fault. These blocks together contain portions of all the major structural units present in the fault zone. The first analyses were performed on a Cameca SX50 electron microprobe capable of wavelength dispersive X-ray spectroscopy (WDS), energy dispersive X-ray spectroscopy (EDS), and backscatter electron (BSE) imaging.

BSE images of 1 mm^2 areas with a 1μm resolution were taken at several locations in each structural unit (Figure 3). Gray scale BSE images are sensitive to the atomic number, *z*, of the material imaged and are helpful in identifying phase contrasts within samples. The images are much higher resolution than optical scans and XRF images, and are used in this study to describe microstructural characteristics of the key units.

WDS analysis provides elemental composition by measuring wavelengths of X-rays emitted by atoms as they interact with an incident electron beam. The WDS detectors are

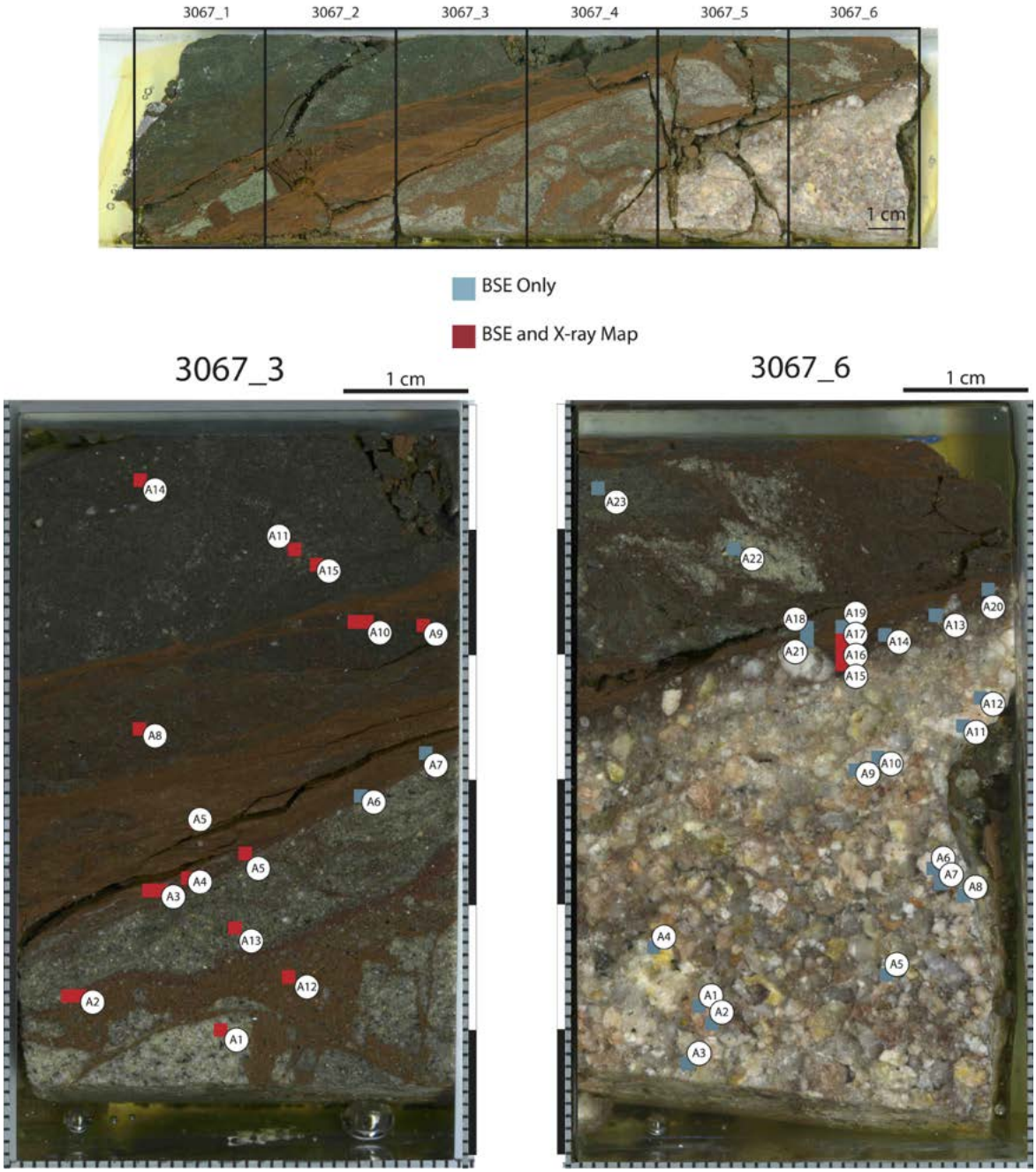

Figure 3: Fault Sample Image and Location of Analyses. (Top) Location of the six blocks cut from the original half-core slab containing the 3067 m MD fault. All blocks were polished and blocks 3 and 6 were carbon coated for electron probe and SEM analyses. (Bottom) Optical scans of blocks 3067_3 and 3067 6 with the locations of BSE images and composite X-ray maps. Locations with BSE and X-ray maps are shown in red, and locations with BSE images only are shown in blue. Smaller squares indicate the location of a 1500x, 63 µm x 63 µm BSE image or X-ray map.

standardized using samples of known composition enabling quantitative compositional analyses at a pixel resolution of 2 μm and an effective resolution of 8 – 10 μm due to effects from the beam interaction volume (R. Guillemette, personal communication, 2014). The incident electron beam interacts with the surface material at the point of contact and also with a volume of surrounding material and material beneath the surface. This phenomenon reduces the effective resolution.

WDS is limited in the number of elements it can detect during a given analysis. For this study, common mineral-forming elements and likely trace elements were selected. The distribution of elements across the sample surface is captured by moving the sample under the beam with the automated stage or by using internal magnets to move the beam over the fixed sample. These analyses yield X-ray maps of the distribution and relative intensity of X-rays for the sampled elements. This is similar to the XRF images used in initial sample description, but with higher resolution and a quantitative description of the composition. X-ray maps were created for Al, Ba, Ca, Fe, K, Mg, Na, P, Si, Sr, Ti, and Zr using a 15 kV 20 nA beam.

The elemental maps were stacked and combined with image processing software (NIH image) to create mineralogical maps of the sample surface called composite X-ray maps. Eight of the twelve elemental X-ray maps were assigned a pixel value, and when these are combined, the combination of the pixel values, yield new pixel values that correspond to the minerals composed of the constituent elements selected. Pixels within an X-ray composite map that only contain the silicon pixel value, for example, are interpreted as quartz. Twenty-three composite X-ray maps were created in areas of

interest within each structural domain (Figure 3). The X-ray maps are displayed with BSE images to compare structural observations with mineralogical data. Imaging processing software ImageJ was used to calculate the percent pixel area represented by each phase in the composite X-ray maps. Mineralogy of the structural units is determined using this method.

The mineralogical data presented represent percentages of each phase that is above the ~5 micron effective resolution of the images composite X-ray maps. The mineralogy of the whole structural unit is represented by several 1 mm x 1mm composite X-ray maps and has an inherent statistical error. This effect is also grain-size dependent in that a large grain in any single image will bias the calculated mineralogy for that image, and subsequently the mineralogy of the zone in which it was captured. The effect is dependent on the image area with respect to the average grain size.

WDS analyses were performed on several feldspar grains within each structural unit to identify the degree of alteration, and any intragranular alteration products. WDS data provide quantitative compositional information of the feldspars used to determine the percent of each feldspar phase present in the feldspar solid solution series. WDS analyses were performed on numerous points within feldspar grains in regions where BSE images were captured (Figure 3). Relative differences in grain brightness in BSE images were used to analyze grains of different phases. EDS point scans were used to confirm the identity of phases before WDS analysis. Data were returned in the form of percent weight oxides for each element selected, which for feldspar analyses are Na, Al, Si, K, Ca, Fe, and Ba. The percent oxides data were normalized to the eight oxygens

present in the feldspar chemical formula to determine the percent composition of albite, anorthite, orthoclase, and celsian. These data were compiled into tables by sample location and structural domain.

3.2 Grain Size Distribution and Shear Localization of the 3067 m MD Fault

3.2.1 Grain Size Distribution and Shear Localization Background

Models and observation of comminution processes in shear zones link deformation processes to expected particle size distributions (Billi, 2005; Keulen et al., 2007; Sammis et al., 1986; 1987). These models differentiate grain scale comminution into constrained and unconstrained models of comminution (Sammis et al., 1987). Constrained comminution is characterized by grain crushing and intragranular tensile fracturing, and unconstrained comminution is characterized by abrasion of grain surfaces (Sammis et al., 1987). These processes yield different grain morphologies as well as distinct particle size distributions (Sammis et al., 1986). With both models, increased localized shear leads to a reduced grain size.

Heron (2011) analyzed particle size distributions within several incipient and small subsidiary faults cutting arkosic sandstone recovered from the western damage zone of the SAF at SAFOD during Phase 1 drilling. The faults studied by Heron (2011) are within a single lithology, but provide a similar geologic and lithological context for analyzing particle sizes of the 3067 m MD fault. The arkosic rock of the 3067 m MD fault is similar to the host rock studied by Heron (2011), and its contribution to the 3067 m MD fault may show similar styles of deformation and alteration. Relative particle size changes, indicative of shear localization, will be used in this study to define shear zone

width for model parameter inputs to estimate frictional heat generation of the 3067 m MD fault.

3.2.2 Grain Size Distribution and Shear Localization Methods

The finest grain particle-size fraction is below the resolution of the imaging capabilities of the electron microprobe so a second set of BSE images were captured at higher magnifications using an FEI Quanta 600 scanning electron microscope (SEM). The two sets of BSE images were used to determine average particle size of surviving host-rock grains in each structural domain of the 3067 m MD fault, down to a particle size of approximately 1 micron. Finer particles exist, and could be characterized using Transmission Electron Microscopy in the future. The images from the microprobe and SEM were used to measure 1D diameter of particles from multiple structural domains. These are used to develop a relative description of the degree of deformation, and to understand zones of deformation concentration. Heron (2011) and Heron et al. (2011a & 2011b) documented grain size in nearby rocks as a function of deformation, which provides context for the particle size analyses herein. Particle size is also used to constrain the shear zone width in the modeling portion of this study. Upper and lower bounds on possible shear zone widths are based on regions of local particle size reduction. 1D measurements of particle diameter and the associated statistics are reported as well.

4. VITRINITE REFLECTANCE ANALYSIS AND NUMERICAL MODELING OF HEATING AND VITRINITE RESPONSE

4.1 Vitrinite Reflectance Geothermometry

4.1.1 Vitrinite Reflectance Background

Vitrinite reflectance analysis is a widely used technique for determining thermal history of sedimentary basins, and more recently to estimate the degree of shear heating on a fault surface during one or more earthquake events (Bustin, 1983; Kitamura et al., 2012; O'Hara, 2004; Sakaguchi et al., 2011; Taylor et al., 1998; Vrolijk & van der Pluijm, 1999). Vitrinite refers to a group of organic particles derived from the cell walls of woody plants (Taylor et al., 1998), and is a ubiquitous component in sedimentary rocks of Devonian and younger ages. As vitrinite is heated, typically due to burial, it matures by shedding water, carbon dioxide, and hydrocarbons resulting in a greater concentration of carbon. Vitrinite maturation is a time and temperature dependent kinetic process and as maturity (carbon concentration) increases particles systematically reflect more incident light (Taylor et al., 1998). The percentage of light reflected (%Ro) can be correlated to maximum temperature and because maturation is a unidirectional process, it is a reliable geothermometer. The Easy%Ro model is a time and temperature dependent model for vitrinite maturation established by Sweeney and Burnham (1990). It is a widely used and experimentally verified model of vitrinite maturation based on the kinetic parameters governing several parallel reactions that contribute to maturation (Sweeney & Burnham, 1990). The model calculates the expected %Ro values given inputs of temperature change over time.

High temperatures associated with frictional heating can dissipate to near background levels in the span of hours to days (Lachenbruch, 1986; Fulton and Harris, 2012) and reaction kinetics may limit the production of a detectable signature from a single heating event. The cumulative effect of numerous heating events may produce a zone of increased reaction products within the region bounding a seismogenic fault core. Kinetic models, such as Easy%Ro, can be used to estimate the magnitude of heating necessary to explain observed reflectance values.

Vitrinite reflectance is measured using a reflected light microscope equipped with a photometer, which measures the percentage of incident light reflected by a vitrinite particle under oil immersion. Another, more recent method uses a calibrated gray scale image captured with incident green light on a reflected light microscope under oil immersion. Reflectance is measured on dispersed particles on a polished intact rock surface or on a polished pellet composed of concentrated organic particles (Taylor et al., 1998). Measurement of a polished rock surface preserves the in-situ spatial relationship of particles and is the method used in this study.

4.1.2 Vitrinite Reflectance Analysis Methods

Vitrinite reflectance measurements were performed on particles within the six polished blocks of the 3067 m MD fault and siltstone chips from 0.3, 0.6, 1.5 and 1.8 m above the fault (samples P1B23_2a, P1B22_1a, P1B21_1a, P1B20_1a). Analyses were completed at the labs of the Canadian Geological Survey, Alberta, in Calgary. The analyses were performed on a Zeiss AxioImage II microscope using the FOSSIL-Discus software system for reflectance analysis from calibrated gray scale images. Analyses

were performed as collaboration with Drs. Hamed Sanei and Omid Ardakani. All observations were taken under reflected light in oil immersion at 500 and 1000 times magnification.

Observation revealed the presence of vitrinitic, bituminous, and inertinitic particles. The majority of the observed organics were vitrinite and bitumin. Organic particles were found almost exclusively in the intact siltstone unit and its clasts. The RBG and BG material adjacent to the siltstone unit contains some organic particles but far fewer than in the intact siltstone. Most particles found in the gouge were microns in diameter with irregular surfaces. Measurement of reflectance values required a smooth surface of at least 0.1 micron in diameter and many particles were too small to accurately measure or lacked sufficiently large, smooth surfaces. Organic macerals were identified and categorized by morphology and optical characteristics under the supervision of Dr. Sanei.

Reflectance measurements were performed first on organic particles within the intact siltstone unit. Particles were measured in several transects away from the shear zone to establish a baseline reflectance value. Particles within three distinct zones (Figure 4) in sample 3067_1 were measured to identify any potential difference in mean reflectance based on structural zones.

Sample 3067_3 (Figure 3) contains a portion of intact siltstone, cataclastic sandstone, and zones of fine-grained matrix, which are separated by sharp contacts. Particles within this sample were measured and their X, Y coordinates recorded to determine any systematic change in reflectance within structural units or with proximity to fine-grained

zones which may have accommodated the greatest strain (Figure 5). The same procedure of measuring reflectance and plotting X, Y locations was performed in sample 3067_6. This latter sample contains a region with siltstone clasts in close proximity to two regions of a very-fine-grained, foliated fault rock zone (Figure 3). Organic matter within three siltstones from the Phase 1 core was collected at 3066 m MD, 3065 m MD, 3064 m MD, and 3063 m MD. These samples were analyzed to establish reflectance values away from the 3067 m MD fault. No organic material could be found in the sample P1B.

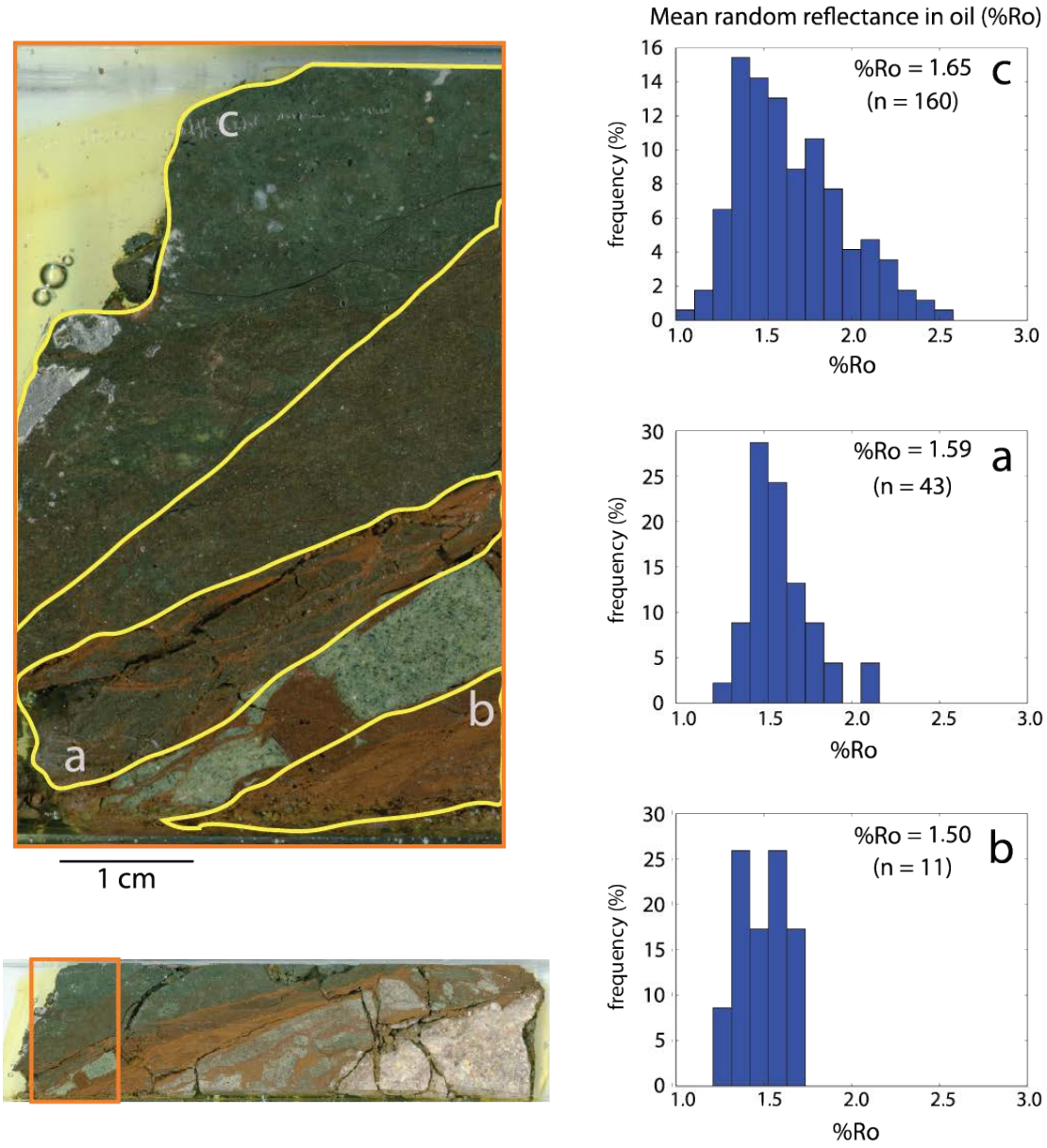

Figure 4: Reflectance by Zone of Sample 3067_1. Histograms and mean reflectance values for populations of vitrinite particles found within three units of block 3067_1. The low n value for area b is due to the lack of organic particles present in the sample.

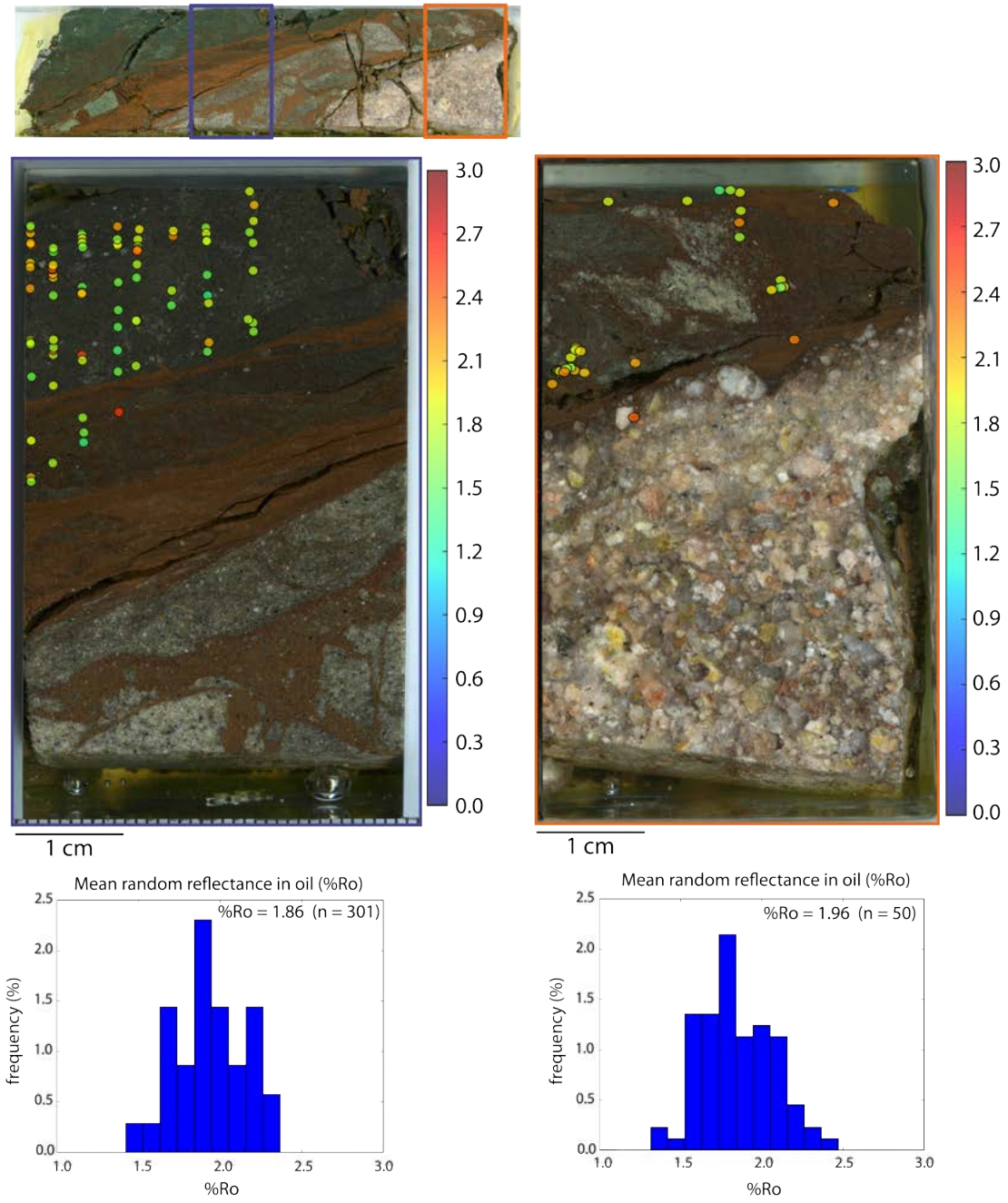

Figure 5: Reflectance and Particle Locations of Samples 3067_3, 3067_6. Optical scans of blocks 3067_3 and 3067_6 showing the sampling locations (circles) of vitrinite particles. The color of the circles corresponds to the average reflectance values of particle at that location. Histograms show the distribution and frequency of reflectance values as well as the mean %Ro for the sampled population. The relatively low n value of the sample on the right is due to the difficulty of finding particles in the sample.

4.2 Numerical Modeling of Frictional Heating and Vitrinite Reflectance

4.2.1 Numerical Modeling Background

The effect of temperature on vitrinite maturation is well documented and can be modeled for varying rates and magnitudes of heating (Fulton & Harris, 2012; Sweeney & Burnham, 1990). The Easy%Ro model can be combined with a model for frictional heat generation and 1D diffusion to determine expected reflectance values near a shear zone (Fulton & Harris, 2012). Lachenbruch (1986) developed a model that incorporates the mechanical properties of faults, slip behavior, and thermal properties of the host rock to model temperature rise and dissipation in the vicinity of shear zones. In this model, temperature, T, is determined as a function of time, t, after initiation of slip and distance, x, from the shear zone center , and is described mathematically by

$$T(x,t) = \frac{A_o}{\rho c}\begin{pmatrix} t\left[1 - 2i^2erfc\left(\frac{a-x}{\sqrt{4\alpha t}}\right) - 2i^2erfc\left(\frac{a+x}{\sqrt{4\alpha t}}\right)\right] \\ -H(t-t^*)(t-t^*)\left[1 - 2i^2erfc\left(\frac{a-x}{\sqrt{4\alpha(t-t^*)}}\right) - 2i^2erfc\left(\frac{a+x}{\sqrt{4\alpha(t-t^*)}}\right)\right] \end{pmatrix} \quad (3)$$

for values of x within the shear zone, and

$$T(x,t) = \frac{A_o}{\rho c}\begin{pmatrix} t\left[2i^2erfc\left(\frac{a-x}{\sqrt{4\alpha t}}\right) - 2i^2erfc\left(\frac{a+x}{\sqrt{4\alpha t}}\right)\right] \\ -H(t-t^*)(t-t^*)\left[2i^2erfc\left(\frac{a-x}{\sqrt{4\alpha(t-t^*)}}\right) - 2i^2erfc\left(\frac{a+x}{\sqrt{4\alpha(t-t^*)}}\right)\right] \end{pmatrix} \quad (4)$$

for values of x outside of the shear zone, where a is shear zone half-width, α is the thermal diffusivity, ρ is the bulk density, c is the heat capacity, t^* is slip duration, i^2erfc is the second integral of the complimentary error function, H is the Heaviside fuction, and

$$A_o = \frac{\tau v}{2a} = \frac{\tau u}{2at^*} \quad (5)$$

where τ is the shear stress, v is the slip velocity, and u is slip magnitude. This more complete model incorporates frictional heat generation and diffusion, and can be paired with the Easy%Ro model to predict reflectance values from heating events (Fulton & Harris, 2012).

Previous work on vitrinite in fault zones (e.g. Bustin, 1983; O'Hara, 2004; Sakaguchi, 2011) has determined that increased reflectance values are common within and adjacent to the shear zone. The reflectance data collected within the 3067 m MD fault and the siltstones adjacent to the fault provide reflectance values immediately adjacent to the shear zones and away from the fault to determine background reflectance values. Additional reflectance data were collected by Kirschner et al. (2006) in the Phase 2 core at depths from 2565 to 2973 m true vertical depth (TVD). The data of Kirschner et al. (2006) established a trend of maturation with depth that is used to understand thermal history of the host rocks and in the case of the 3067 m MD fault, to identify reflectance values suggesting maturation in excess of expected values from burial.

Models of frictional heat generation and diffusion through nearby host rock (equations 3, 4) provide estimates of the magnitude of frictional heat that is generated from fault slip. Experimentally derived values of frictional properties (Tembe et al., 2006; Kitajima et al., 2013) and estimates of the in-situ state of stress (Hickman & Zoback, 2004; Tembe et al., 2009) are used to model frictional heat generation. The possible orientations of the 3067 m MD fault (Almeida et al., 2005; Chester et al., 2006; Almeida, 2007) are used to estimate the maximum possible normal and shear stresses on the fault plane, and the maximum possible frictional heat generation.

Maximum temperature and residence time of heating is modeled at a given position in or away from a fault zone. The temperature data are used as an input for the Easy%Ro model which then yields the expected reflectance value for vitrinite at a given distance from a shear zone at time, *t,* following a heating event (e.g., Fulton & Harris, 2012). Microscopic mapping of individual vitrinite particles and mapping of shear zones are used to identify any trend in reflectance values as a function of structural domain or proximity to any observable textures indicating possible shear localization.

Published values of the geothermal gradient and age estimates of the arkosic rocks at SAFOD (e.g., Springer et al., 2009; Williams, 2004) were used with the Easy%Ro model to determine the expected vitrinite reflectance values due to burial assuming a range of geothermal gradients from literature. Reflectance values for the 3067 m MD fault and the locations from Kirschner et al. (2006) were modeled with the Easy%Ro model to determine the extent of agreement between modeled and observed data. The model of frictional heating and diffusion was coupled with the Easy%Ro model in the style of Fulton et al. (2012) and Kitamura et al. (2012) to estimate the slip characteristics and subsequent temperature rise that would be required to explain varying degrees of vitrinite maturation. Maturation is greatly dependent on maximum temperature and to a lesser extent heating time (Burnham & Sweeney, 1989). Temperature rises and residence times associated with seismic rupture are measured on the order of seconds to days, and at short time scales, a greater temperature rise is necessary to produce a detectable signature in vitrinite reflectance than for geologic time scales.

4.2.2 Numerical Modeling Methods

This study follows the methods of Fulton and Harris (2012) in which numerical models of shear heating, thermal diffusion, and subsequent vitrinite maturation were used to explain observed %Ro values in fault gouge. Appropriate parameters for the modeling in this study will be chosen to reflect the unique conditions of the 3067 m MD fault. Based on observed values of vitrinite reflectance, known in-situ conditions at the sampled depths, and models of shear heating mechanics and vitrinite maturation kinetics, an inverse problem is modeled to constrain the unknown parameters capable of producing observed %Ro values as a proxy for maximum temperature from faulting. In the case of the 3067 m MD fault, the unknown parameters include slip duration, slip magnitude, fault plane orientation, and frictional coefficients.Equations 4, 5, and 6 are the basis of modeling frictional heat generation and diffusion in the fault rock. Model parameters are specified in Table 1. Values for normal and shear stress along the fault were modeled using estimates of the stress tensor at depth from Hickman and Zoback (2004), though stress magnitudes and orientations were not sampled at the depth of the 3067 m MD fault. A linear trend with depth for both magnitude and orientation of the horizontal stress components was assumed to extrapolate for the in-situ stresses at depth (Figures 6, 7). The stress orientations derived in this manner from Hickman and Zoback (2004), based on a burial depth of 2558 m TVD, are plotted on a lower-hemisphere stereographic projection along

True Vertical Depth Present Day (m)	2558
Max True Vertical Depth (m)	4263
Max Paleo Temperature °C	170
Age Ma (max)	65
Age Ma (min)	35
Geothermal gradient °C/km	35
Present Surface Temperature °C	20
Present Temperature at TVD °C	110
Bulk Density (kg/m^3)	2367
Normal Stress on fault plane (Mpa)	85
Coefficents of Friction	0.4, 0.6
Porosity (from bulk density) Vp/Vt	0.172
Thermal Conductivity, K, W m-1 K-1	2.4
Specific Heat Capacity, Cp, J/kg K	840.00
Thermal Diffusivity, m^2 sec-1	1.21E-06
Half-widths of shear zone, a (m)	0.00025, 0.005
Slip durations, t* (s)	0.01, 0.015, 0.02, 0.025, 0.03, 0.035, 0.04, 0.045, 0.05
Slip magnitudes, u (m)	0.01, 0.015, 0.02, 0.025, 0.03, 0.035, 0.04, 0.045, 0.05

Table 1: Modeling Inputs for Frictional Heating and Maturation Models.
Parameters used in modeling shear zone heating and vitrinite maturation response (Eppelbaum et al., 2014; Springer et al., 2009).

with the estimates of stress orientations from Almeida, et al. (2005) and Chester et al. (2006) (Figure 8)**.** The two methods show general agreement and thus the magnitudes of stresses are taken from Hickman and Zoback (2004) and assumed to be in the orientations estimated by Almeida et al. (2005) and Chester et al. (2006) because these provide a three dimensional estimate of the stress state. The mapping of the 3067 m MD fault by Chester et al. (2006) gives the possible orientations of the 3067 m MD fault plane with respect to the SAFOD bore hole. The small circle in Figure 8 is a plot of all possible orientations of the normal to the fault. These orientations were sampled for numerical modeling in 10-degree increments. Each of the 36 possible orientations was rotated into the coordinate system of the stress tensor estimated from Hickman and Zoback (2004), Almeida et al. (2005), and Chester et al. (2006). This derived stress tensor is used to resolve the normal and shear stresses across each of the possible fault plane orientations (Figure 8). Published estimates of the maximum burial temperature and the geothermal gradient (Springer et al., 2009) are used to determine the maximum burial depth and corresponding stress magnitudes for the 3067 m MD fault before uplift to its current TVD. The maximum possible values of shear and normal stress are then used as inputs to the shear-heating model to determine maximum possible frictional heating. Kitajima et al. (2006) performed high-speed friction tests on gouge material from the 3067 m MD fault and determined a coefficient of friction, μ, of ~0.4 for the natural gouge material. This value is used for all modeling. Published values for thermal properties of arkosic sandstones (Eppelbaum et al., 2014) similar to those bounding the 3067 m MD fault are used where directly measure properties are not available (Table 1).

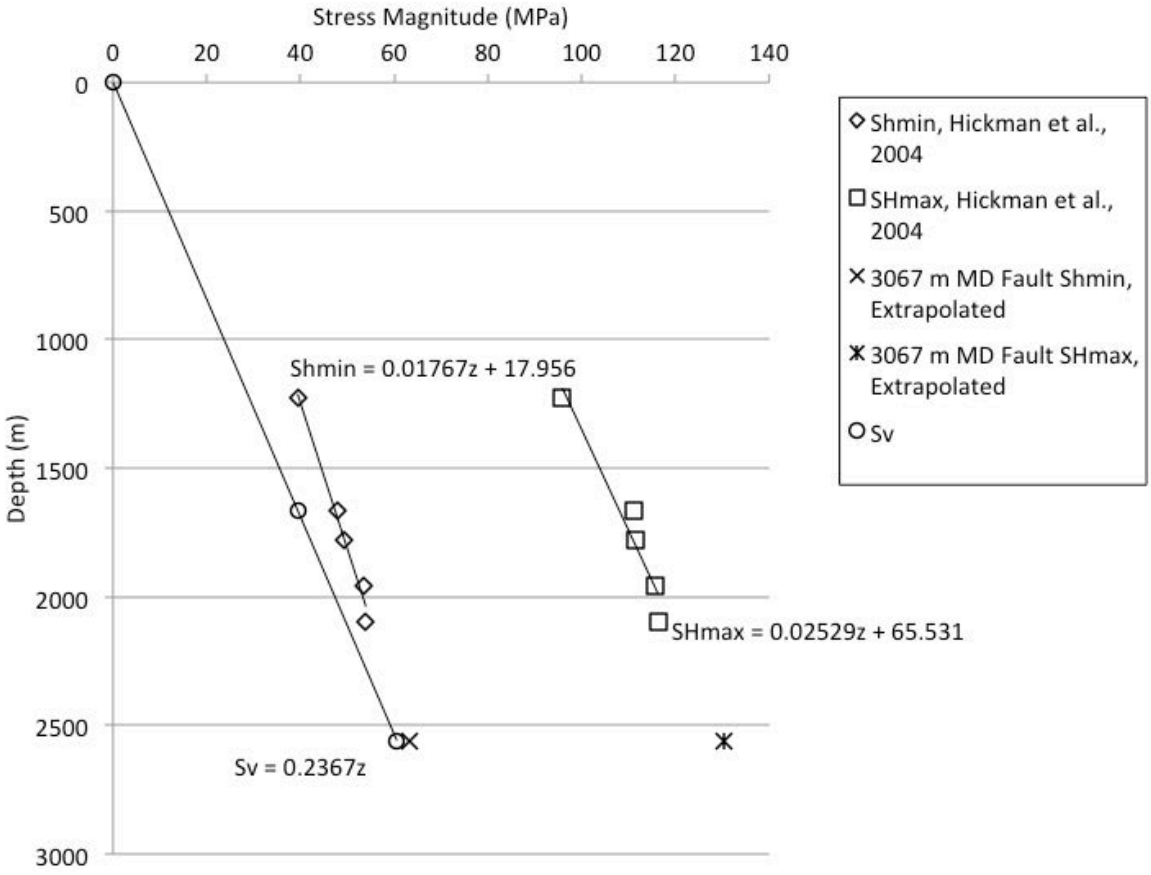

Figure 6: Empirical Stress Magnitude Trend with Depth. Sh min, SH max, and Sv values from Hickman and Zoback (2004) are plotted and used to define a linear trend of stress magnitude with depth. These trends are used to extrapolate for stress magnitudes at the present TVD of the 3067 m MD fault, and for the stress magnitudes at the maximum burial depth of the of the 3067 m MD fault (not shown). These stress magnitudes are the basis for the stress tensor used to compute shear and normal stress, and subsequent heating during coseismic slip.

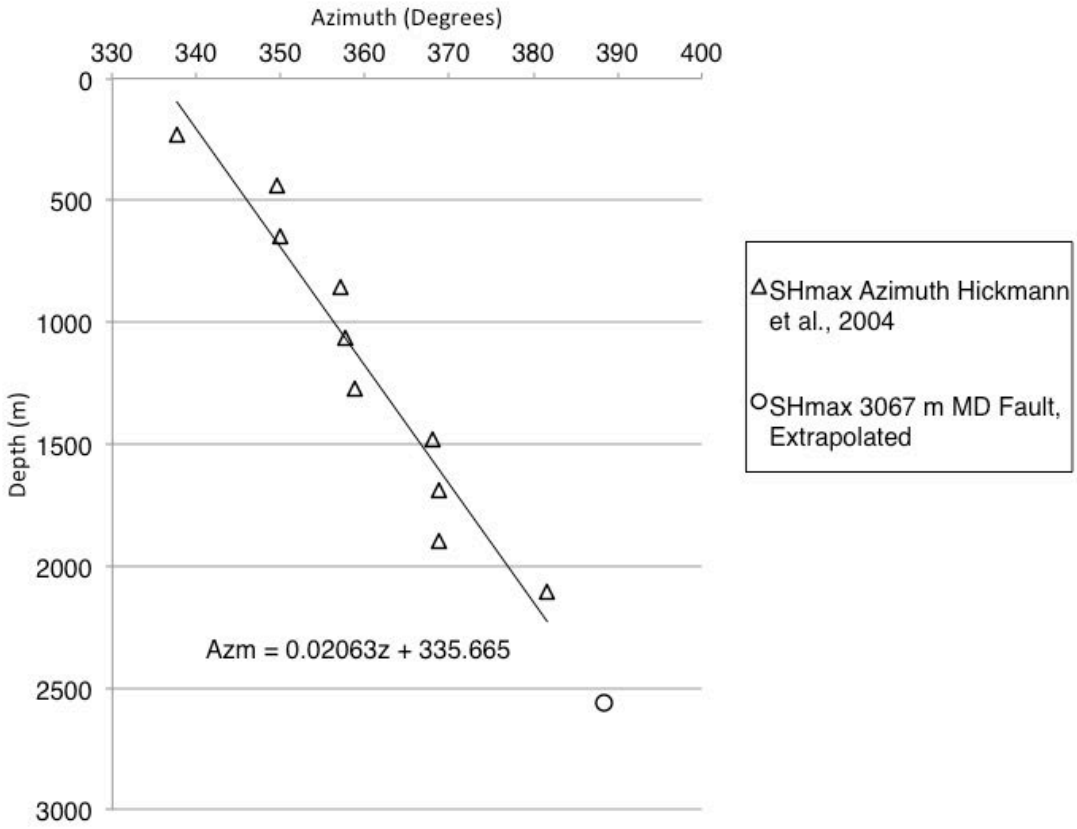

Figure 7: Empirical Stress Orientation Trend with Depth. Sh min, SH max, and Sv values from Hickman and Zoback (2004) are plotted and used to define a linear trend of stress orientation with depth. This trend is used to extrapolate for stress orientation at the present TVD of the 3067 m MD fault, and for the stress magnitudes at the maximum burial depth of the of the 3067 m MD fault (not shown). This stress orientation is the basis for the coordinate system used to compute shear and normal stress, and subsequent heating during coseismic slip.

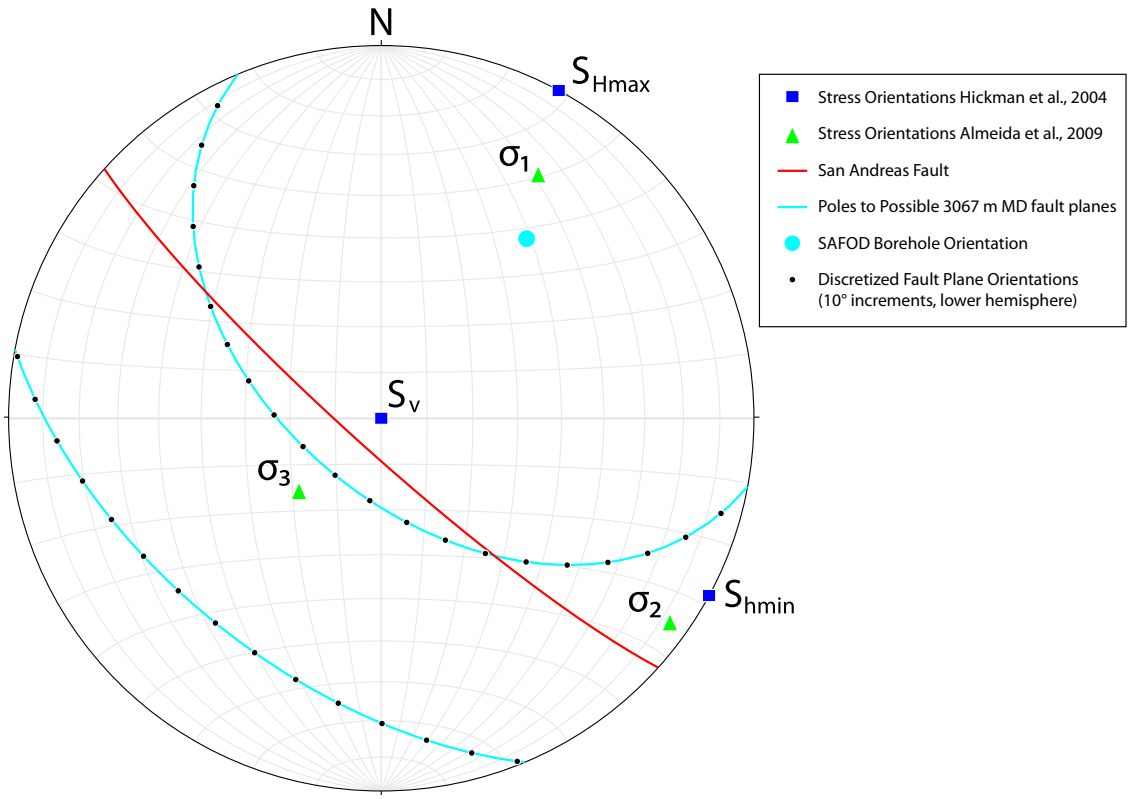

Figure 8: Stereonet of Stress, Borehole, and Fault Orientations. Principal stress orientations from Almeida et al., 2007 along with SHmax and Shmin orientations from Hickman and Zoback (2004). Cyan small circle contains the normals of all possible orientations of the 3067m MD fault by rotation about the axis of the the SAFOD borehole at the point of intersection. Orientation of the SAFOD borehole is shown by the cyan dot. Black dots along this circle represent discretized points (every 10 degrees) used in this study for determination of stresses on potential fault plane orientations. This figure was created using Stereonet 9.2.3 (Allmendinger & Cardozo, 2013).

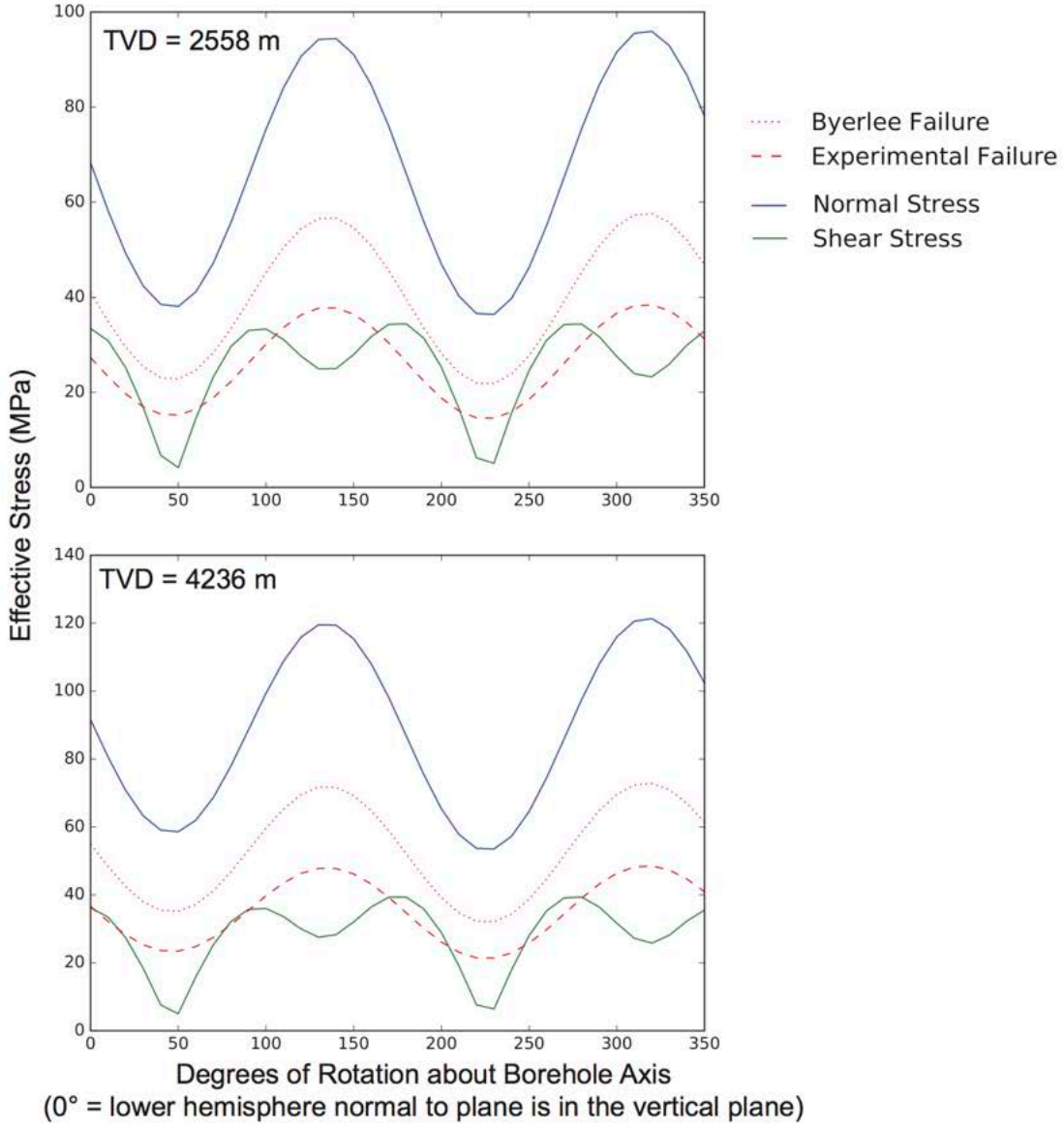

Figure 9: Stress Resolved on the 3067 m MD Fault by Orientation. Effective normal and shear stress on the possible orientations of the 3067 m MD fault. Possible fault and principal stress orientations are from Almeida et al., 2007 and stress component magnitudes are from Hickman et al., 2004. Effective stress calculations assume normal hydrostatic pore pressure. Failure for Byerlee's (1978) and other experimentally derived criteria of $\mu = 0.6$ and $\mu = 0.4$ respectively are plotted to show orientations in which failure would be expected given changing shear stress across the fault plane.

Shear heating from faulting and subsequent diffusion is then modeled with these inputs to calculate temperature as a function of time after slip initiation, mechanical properties of the fault, distance from the shear zone center, and slip magnitude. Observations from the 3067 m MD fault samples provide the upper and lower bounds on the shear zone half-width, *a,* which in this study are 0.005 m and 0.00025 m respectively. Shear heating is modeled for slip magnitudes, *u*, between 0.01 to 0.05. Vitrinite particles outside the shear zone (x > a) mature due heat diffusion into the surrounding host rock. Models of maximum temperature for varying slip magnitudes as a function of distance from the shear zone center, x, are created along with the modeled vitrinite response over the same spatial interval. The starting vitrinite values before slip are determined using the Easy %Ro model assuming maximum temperature from burial of 170° C (Springer et al., 2009).

Sweeney and Burnham (1989) suggest that maximum temperature, T, is the dominant control on %Ro though reaction kinetics require greater temperatures for maturation at time scales of seconds or less as may be encountered from shear heating (Burnham & Sweeney, 1989; Sweeney & Burnham, 1990). Fulton and Harris (2012) demonstrate, through modeling of frictional heating and vitrinite response for multiple events, that %Ro is insensitive to the number of earthquakes because vitrinite reflectance records the single highest temperature (Burnham & Sweeney, 1989; Fulton & Harris, 2012). This study models shear heating and vitrinite response for single events.

Expected initial vitrinite values also control kinetics. For purposes of this modeling, initial vitrinite reflectance values are assumed to be due to maturation from burial.

Draper-Springer et al. (2009) determined a maximum burial temperature of 170 °C. The starting point for all modeling begins with modeling the maturation response of a linear increase in temperature from a surface temperature of 20 °C to 170 °C over 65 million years which yields a starting %Ro value of 1.27%.

5. RESULTS

5.1 Definition and Description of Structural Units Within the 3067 m MD fault

The fault zone displays six optically distinguishable structural units: host arkosic sandstone, cataclastic sandstone, host siltstone, cataclastic siltstone, red-brown gouge, and brown gouge. The six units vary in lithology, mineralogy, degree of deformation, grain size, fabric, and color. The units are defined and characterized at the meso-scale using high-resolution (6400 dpi) optical scans and low-resolution (254 dpi) X-ray fluorescence (XRF) scans, and on the basis of XRD data collected by Kitijima et al. (2006). In the following, descriptions of the structural units are given with respect to the orientation of the fault as shown in Figure 10, with the host siltstone (Unit a) in the upper left corner of the image and the host arkosic sandstone (Unit b) in the lower right corner of the image. Subsequent descriptions of the 3067 m MD fault refer to six structural units labeled in Figure 10: host siltstone, Slt, cataclastic siltstone, cSlt, red-brown gouge RBG, cataclastic sandstone, cSS, and cataclastic sandstone matrix, cSS(m), brown gouge, BG, and the host arkosic sandstone, HAS.

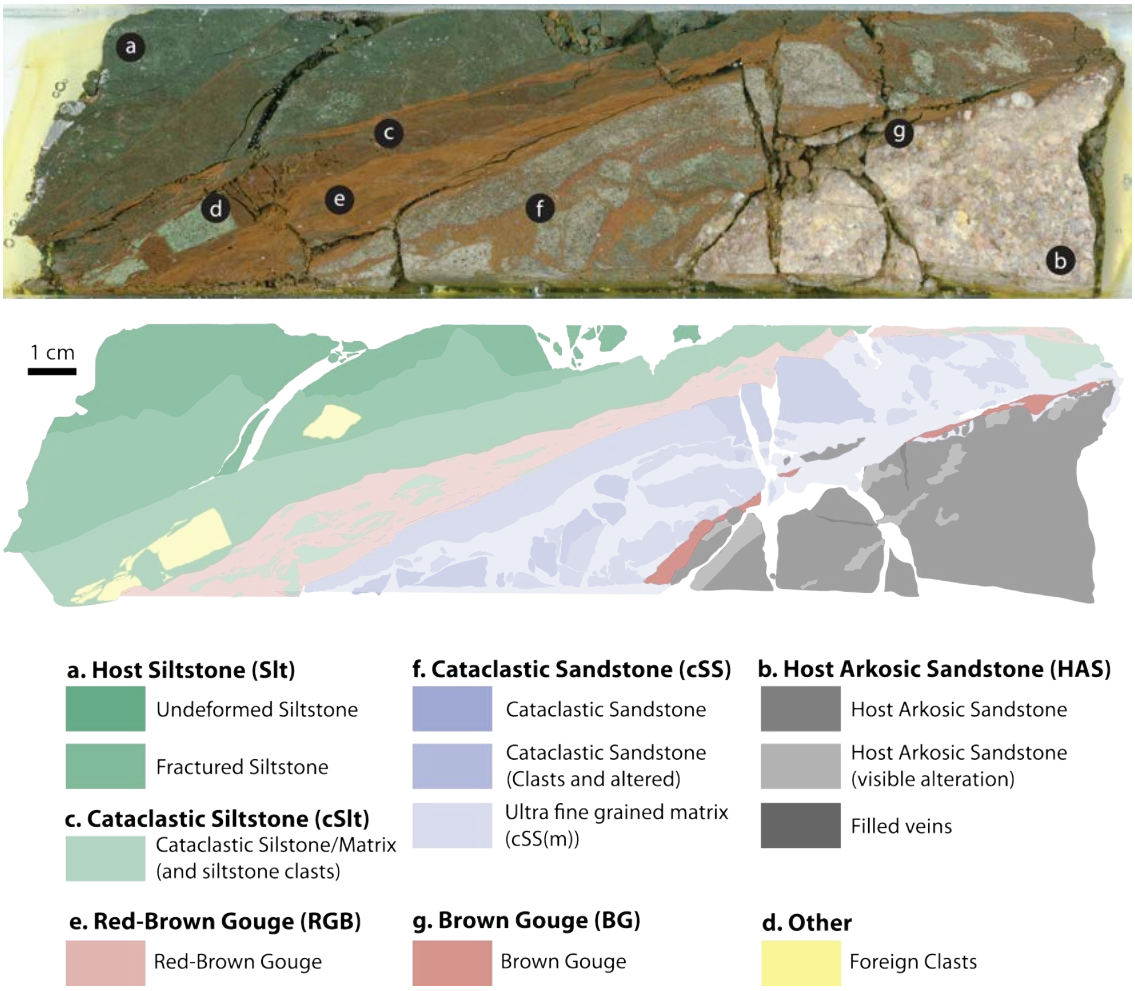

Figure 10: Structural Units of the 3067 m MD Fault. Distinct structural units were mapped within the 3067 m MD fault based on mineralogy, texture, and elemental and mineralogical composition.

5.1.1 Host Siltstone (Slt)

The mineralogy of the siltstone immediately above the 3067 m MD fault was studied by Solum et al. (2006) and Schleicher et al. (2009b) via quantitative XRD analyses and other analytical techniques. These data were coupled with kinetic models of clay phase crystallization to determine the diagenetic origin of the clays. These data provide an accurate background mineralogy for the host siltstone, and coupled with results from Heron (2011) and Springer et al. (2009), provide mineralogical and petrological context for the 3067 m MD fault. For the sample of the fault shown in Figure 10, the Slt unit (a, in Figure 10) is dark green to grey in color and does not show foliation or obvious visual signs of shear deformation at the hand sample scale. It is a well-sorted siltstone matrix of indistinguishable particles with a few dispersed, light-colored grains that are up to 1 mm in diameter. Based on the XRF scans reported herein, the major mineral-forming elements of the host siltstone are Al, Ca, Fe, K, and Si (Figure 10**)**. Ca and Fe are less abundant in the Slt unit relative to the other structural units, with Fe X-ray fluorescence increasing towards the fault. The light-colored, larger particles are composed of Silicon and assumed to be quartz grains. These larger quartz grains are visible in several regions across the Slt unit. A few matrix-filled fractures cut the Slt.

5.1.2 Cataclastic Siltstone (cSlt)

The Slt forms a sharp contact with the cSlt unit (c, in Figure 10), a zone of significantly greater deformation that is characterized by an increase in fracture density and siltstone clasts towards the fault core surrounded by dark brown, fine-grained matrix. The transition is marked by an increase in fracture density and fine-grained

material producing a region of siltstone clasts and matrix-filled fractures. There are also several mm to cm scale clasts (d, in Figure 10) of fine-grained sandstone within the fine-grained matrix of the cSlt unit. The fractures within the cSlt are predominantly parallel and sub-parallel to the fault. Some of the matrix material within the wider fractures shows minor foliation fabric. XRF scans and composite X-ray maps show a pronounced increase in Fe content relative to the Slt and high Fe values are present within some of the fracture fill (Figure 11).

5.1.3 Red-Brown Gouge (RBG)

The cSlt forms a sharp contact with the RBG (e, Figure 10). The RBG is ultra fine-grained and shows a distinct fabric characterized by anastomosing bands of slight color variation. Numerous elongate lozenges of brown and green siltstone are embedded within the RBG, and elongate lozenges of fine, cataclastic sandstone are present in the RBG within ~1 mm of the boundary with the cSlt unit. Fractures within the RBG domain are predominantly fault-zone-parallel or oblique (~30°) to and truncating against the fault-zone-parallel fractures. This unit is juxtaposed at a sharp contact against a zone composed of clasts of fine-grained cataclastic sandstone (f, in Figure 10). The XRF signature of the RBG is similar in its elemental composition to the Slt, but shows a much higher concentration of Fe. The most striking feature of the RBG in XRF images is the sharp contact with the cSS.

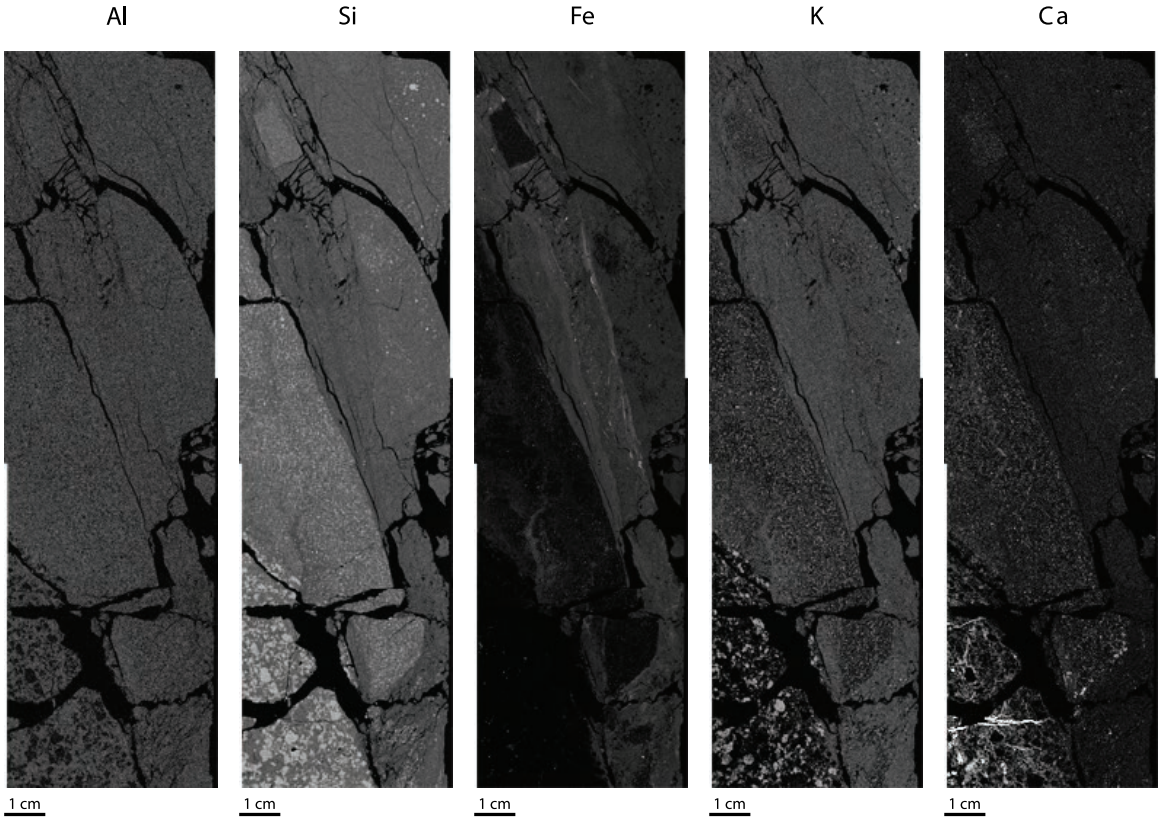

Figure 11: X-Ray Fluorescence Images of the 3067 m MD Fault Zone. X-ray fluorescence images with 100 μm resolution of the 3067 m MD fault showing the common mineral-forming elements represented in the fault. Images are composed of four 5.12 cm x 5.12 cm overlapping scans taken along the fault and digitally combined.

5.1.4 Cataclastic Sandstone (cSS)

The cSS unit (f, in Figure 10) contains an ~11 cm long group of elongate sandstone clasts at the boundary with the RBG and several other sandstone clasts, millimeters to tens of millimeters in diameter. The clasts are composed of fine-grained sandstone and surrounded by light-brown matrix material (cSS(m)). The cSS(m) is similar in color to the RBG but contains numerous light-colored grains up to 1 mm in diameter and does

not show any foliation fabric. The cSS(m) material shows a distinct red color in several regions where the cSS(m) material meets the cSS clasts. The cSS is enriched in Ca and Si relative to the RBG and Slt regions of the fault and shows very little Fe and lower levels of K. The cSS(m) is distinct from the cSS clasts in XRF images and shows a greater concentration of Fe and K and slightly higher Ca.

5.1.5 Brown Gouge (BG)

A narrow band (1-5 mm) (g, in Figure 10) similar in appearance to the RBG separates the cSS unit from the HAS. It is discontinuous across the sample likely due to secondary damage to the sample from coring and recovery. The BG shows foliation and an ultra-fine grain size and is similar in appearance to the RBG. The BG contains sub-rounded to sub-angular survivor grains of plagioclase, potassium feldspar, and quartz. The XRF signature of the BG is very similar to the RBG as well and shows high iron content in contrast to low iron content in the HAS. The boundary between the BG and the HAS is very sharp in both optical and XRF images.

5.1.6 Host Arkosic Sandstone (HAS)

The cored sample of the 3067m fault captured several large clasts of the HAS (a, in Figure 10), which are separated by open, epoxy-filled fractures. The HAS is well sorted and composed of large felsic grains up to ~5 mm in diameter. Optically there is little evidence of alteration and deformation other than a few regions showing a darker color and slightly smaller grain size. Grains of feldspar and quartz are optically identifiable, and calcite vein fill was identified in XRF scans. Fine-grained material is found at the

contact between the HAS and the BG. XRF scans show Al, Ca, K, and Si as the major elements with minor amounts of P and Ti.

5.2 Mineralogy of the 3067 m MD Fault

Mineralogy of each domain was determined by measuring the percent pixel area of each phase in composite X-ray maps created within each structural unit. The values calculated from each X-ray map were grouped by structural unit and averaged. The percent pixel area by phase is given for each composite X-ray map and averaged for each structural unit in Tables 2 and 3.

Evidence of alteration increases towards the fault core of the 3067 m MD fault shown by decreasing grain size, and increasing percentage of alteration products, but the alteration products are distinct from those found 5 to 10 meters shallower in the borehole where the samples studied by Heron (2011) were collected. Percentages are reported for quartz, albitic plagioclase (low Ca), plagioclase (andesine/oligoclase), orthoclase, distinguishable clay phases (illite, illite-smectite), apatite, calcite, high-iron, and epidote/laumontite/calcic phases are reported for each image and each structural unit (Tables 2 and 3). Indistinguishable phases are reported as 100% - the sum of the reported phases. BSE images and composite X-ray maps, along with the locations of each analysis are shown in Figures 12, 13, and 14.

Image Domain	bl3A01 cSS	bl3A13 cSS	bl3A02 cSS/cSS(m)	bl3A12 cSS(m)	bl3A03 cSS/RBG	bl3A03s cSS/RBG	bl3A04 cSS/RBG	bl3A05 cSS/RBG	bl3A05s RBG	bl3A07s RBG	bl3A08 cSlt	bl3A09 cSlt	bl3A10 cSlt	bl3A15 Slt/cSlt	bl3A11 Slt	bl3A14 Slt	bl6A15 HAS/BG	bl6A16 HAS/BG	bl6A16s HAS/BG	bl6A17 BG	bl6A17s BG	bl6A19s BG
apatite	1.4%	1.0%	1.6%	2.4%	2.7%	15.4%	2.0%	2.0%	1.4%	1.4%	2.0%	1.0%	2.3%	1.4%	1.7%	1.3%	1.7%	2.1%	3.5%	1.7%	4.0%	4.1%
quartz	21.4%	17.6%	15.1%	3.0%	11.8%	0.7%	12.0%	11.8%	1.7%	0.0%	4.1%	4.4%	10.3%	6.4%	8.1%	3.7%	14.3%	4.7%	0.5%	1.8%	0.1%	0.8%
I/S	4.6%	9.3%	10.8%	21.8%	16.5%	23.4%	19.1%	25.4%	32.3%	28.6%	31.7%	33.5%	25.9%	24.4%	22.1%	34.8%	18.8%	22.8%	39.0%	28.0%	33.3%	21.9%
calcite	0.0%	0.0%	0.0%	0.0%	0.0%	0.0%	0.0%	0.0%	0.0%	0.0%	0.0%	0.1%	0.0%	0.0%	0.0%	0.0%	0.0%	0.0%	0.0%	0.0%	0.0%	0.0%
epidote/laum/calc	0.7%	1.0%	2.1%	6.1%	1.4%	4.1%	2.1%	1.6%	0.4%	0.3%	0.9%	1.3%	1.3%	1.1%	1.6%	0.8%	1.9%	0.6%	0.2%	1.4%	0.7%	1.0%
albitic plag	11.0%	6.7%	8.4%	7.7%	9.1%	4.4%	5.2%	5.1%	2.3%	3.5%	6.2%	5.6%	4.4%	6.5%	7.8%	4.4%	10.0%	8.4%	3.7%	7.6%	3.1%	5.1%
plag	27.7%	27.4%	19.5%	15.4%	8.3%	3.1%	9.4%	7.6%	6.6%	5.2%	10.0%	9.5%	8.7%	14.5%	13.3%	8.6%	13.5%	12.3%	3.6%	6.1%	1.2%	1.5%
illite	7.5%	5.9%	7.4%	5.3%	10.8%	5.7%	8.4%	8.0%	6.2%	6.8%	10.0%	10.1%	7.1%	9.6%	9.4%	10.4%	5.3%	4.7%	5.6%	7.3%	9.6%	2.7%
Hi-Fe	2.1%	0.2%	0.3%	0.5%	0.1%	0.5%	0.6%	1.3%	0.5%	0.1%	1.2%	1.9%	7.2%	0.0%	2.4%	0.3%	2.7%	2.7%	1.4%	0.9%	0.7%	0.5%
K-spar	10.5%	15.2%	11.9%	8.6%	4.5%	3.7%	5.4%	2.4%	5.8%	12.5%	4.5%	3.7%	2.8%	6.1%	10.9%	3.5%	9.2%	11.8%	3.4%	6.0%	2.4%	2.7%
Total	86.8%	84.3%	77.0%	70.7%	65.1%	61.0%	64.2%	65.2%	57.1%	58.4%	70.8%	71.1%	69.8%	70.1%	77.3%	67.9%	77.5%	70.0%	61.0%	60.7%	55.1%	40.3%
quartz	21.4%	17.6%	15.1%	3.0%	11.8%	0.7%	12.0%	11.8%	1.7%	0.0%	4.1%	4.4%	10.3%	6.4%	8.1%	3.7%	14.3%	4.7%	0.5%	1.8%	0.1%	0.8%
albitic plag	11.0%	6.7%	8.4%	7.7%	9.1%	4.4%	5.2%	5.1%	2.3%	3.5%	6.2%	5.6%	4.4%	6.5%	7.8%	4.4%	10.0%	8.4%	3.7%	7.6%	3.1%	5.1%
plagioclase	27.7%	27.4%	19.5%	15.4%	8.3%	3.1%	9.4%	7.6%	6.6%	5.2%	10.0%	9.5%	8.7%	14.5%	13.3%	8.6%	13.5%	12.3%	3.6%	6.1%	1.2%	1.5%
orthoclase	10.5%	15.2%	11.9%	8.6%	4.5%	3.7%	5.4%	2.4%	5.8%	12.5%	4.5%	3.7%	2.8%	6.1%	10.9%	3.5%	9.2%	11.8%	3.4%	6.0%	2.4%	2.7%
clays	12.0%	15.2%	18.2%	27.0%	27.2%	29.1%	27.5%	33.4%	38.5%	35.4%	41.7%	43.7%	33.0%	34.0%	31.5%	45.2%	24.2%	27.5%	44.7%	35.3%	42.9%	24.5%
indistinguishable	13.2%	15.7%	23.0%	29.3%	34.9%	39.0%	35.8%	34.8%	42.9%	41.6%	29.2%	28.9%	30.2%	29.9%	22.7%	32.1%	-9.2%	30.0%	39.0%	39.3%	44.9%	59.7%
Total	95.9%	97.8%	96.0%	91.0%	95.8%	80.1%	95.3%	95.1%	97.7%	98.3%	95.8%	95.7%	89.3%	97.5%	94.3%	97.6%	62.0%	94.6%	94.9%	96.0%	94.6%	94.3%

Table 2: Mineralogy of Composite X-Ray Maps. Mineralogy of each sample location and its corresponding fault zone domain. The upper table breaks out individual phases, while the lower table combines minerals into groups. The (m) distinction is for the matrix portion of the associated fault zone domain. Samples with two zones in the column header (e.g. HAS/BG) were collected at the boundary of the two zones.

	HAS/BG	BG	cSS	cSS/cSS(m)	cSS/RBG	RBG	cSlt	cSlt/Slt	Slt	Avg
apatite	2.4%	3.3%	1.2%	2.0%	5.5%	1.4%	1.8%	1.4%	1.5%	2.1%
quartz	6.5%	0.9%	19.5%	9.0%	9.1%	0.8%	6.2%	6.4%	5.9%	8.1%
I/S	26.9%	27.7%	6.9%	16.3%	21.1%	30.4%	30.4%	24.4%	28.5%	22.6%
calcite	0.0%	0.0%	0.0%	0.0%	0.0%	0.0%	0.0%	0.0%	0.0%	0.0%
calcic plag + Fe	0.9%	1.0%	0.9%	4.1%	2.3%	0.3%	1.2%	1.1%	1.2%	1.6%
albitic plag	7.4%	5.2%	8.9%	8.0%	6.0%	2.9%	5.4%	6.5%	6.1%	6.3%
plagioclase	9.8%	2.9%	27.6%	17.5%	7.1%	5.9%	9.4%	14.5%	10.9%	13.3%
illite	5.2%	6.5%	6.7%	6.3%	8.2%	6.5%	9.1%	9.6%	9.9%	8.0%
Hi-Fe	2.3%	0.7%	1.1%	0.4%	0.6%	0.3%	3.4%	0.0%	1.3%	1.0%
K-spar	8.1%	3.7%	12.8%	10.2%	4.0%	9.1%	3.7%	6.1%	7.2%	7.6%
indistinguishable	30.5%	48.0%	14.5%	26.2%	36.1%	42.2%	29.4%	29.9%	27.4%	29.4%
Total	**100.0%**	**100.0%**	**100.0%**	**100.0%**	**100.0%**	**100.0%**	**100.0%**	**100.0%**	**100.0%**	**100.0%**

	HAS/BG	BG	cSS	cSS/cSS(m)	cSS/RBG	RBG	cSlt	cSlt/Slt	Slt	Avg
quartz	6.5%	0.9%	19.5%	9.0%	9.1%	0.8%	6.2%	6.4%	5.9%	8.1%
albitic plag	7.4%	5.2%	8.9%	8.0%	6.0%	2.9%	5.4%	6.5%	6.1%	6.3%
plagioclase	9.8%	2.9%	27.6%	17.5%	7.1%	5.9%	9.4%	14.5%	10.9%	13.3%
orthoclase	8.1%	3.7%	12.8%	10.2%	4.0%	9.1%	3.7%	6.1%	7.2%	7.6%
clays	32.1%	34.2%	13.6%	22.6%	29.3%	36.9%	39.5%	34.0%	38.4%	30.6%
indistinguishable	36.1%	53.0%	17.6%	32.7%	44.5%	44.3%	35.8%	32.5%	31.5%	34.1%
Total	**100.0%**	**100.0%**	**100.0%**	**100.0%**	**100.0%**	**100.0%**	**100.0%**	**100.0%**	**100.0%**	**100.0%**

Table 3: Mineralogy of Structural Domains from X-Ray Maps. Mineralogy of each distinct domain within and bounding the shear zone from all sample locations within each zone. The upper table breaks out individual phases, while the lower table combines minerals into groups. The (m) distinction is for the matrix portion of the associated fault zone domain. Samples with two zones in the column header (e.g. HAS/BG) were collected at the boundary of the two zones.

The HAS was not documented with composite X-ray maps due to the very coarse grain size that inhibited producing an average mineralogical description. Samples noted as HAS/BG in tables 2 and 3 denote that the X-ray map was captured on the boundary of the HAS and BG zones. Mineralogy of the HAS was determined qualitatively using XRF scans, BSE images, and EDS point analyses. XRF analyses do not produce the same level of excitation and secondary X-ray production as electron beam instruments, and resolving low-atomic-number elements is difficult. This prevented the creation of meaningful XRF images for elements including sodium, without which, it was not possible to discriminate between laumontite, calcic plagioclase, and calcium bearing clay phases. EDS point analyses and contrast and morphology of particles in BSE images were used to confirm the presence and general distribution of laumontite in the host arkose. Heron (2011) reports an increase in laumontite content with increasing deformation up to a maximum of 66% in the highest strain zones. The HAS contains the greatest laumontite content, predominantly present as cement and fracture fill. Laumontite becomes scarce with proximity to the BG zone.

The cSS unit is composed of 19.5% quartz, 8.9% albitic plagioclase, 27.6% other plagioclase, 12.8% orthoclase, 13.6% clay phases, and 14.5% indistinguishable phases (Tables 2 and 3). The fine-grained matrix zone within the cSS, the cSS(m), is reported separately from the cSS due to the fine grain size which increases the percentage of indistinguishable particles. The average grain size of the cSS is 124 μm (Table 4). Feldspar grains within the sandstone show a pitted texture and intragranular phase

contrasts (Figure 12), often in parallel lineations. Grains within the cSS zone are angular and blocky and show extensive intragranular fracturing.

	Slt	cSlt	cSS/RBG	RBG (SEM)	cSS(m)	cSS	HAS/BG
Avg	26.77	24.98	26.99	13.00	51.80	123.90	29.02
Max	89.00	88.00	133.00	84.00	352.00	434.00	96.00
Min	3.00	8.00	6.00	3.00	9.00	14.00	9.00
Std	17.45	15.00	23.75	12.11	63.69	105.79	16.69

Table 4: Particle Sizes by Structural Domain. Statistics of particle size populations (average, maximum, minimum, standard deviation) for each structural domain. Particle size is reported in microns. Samples with two zones in the column header (e.g. HAS/BG) were collected at the boundary of the two zones.

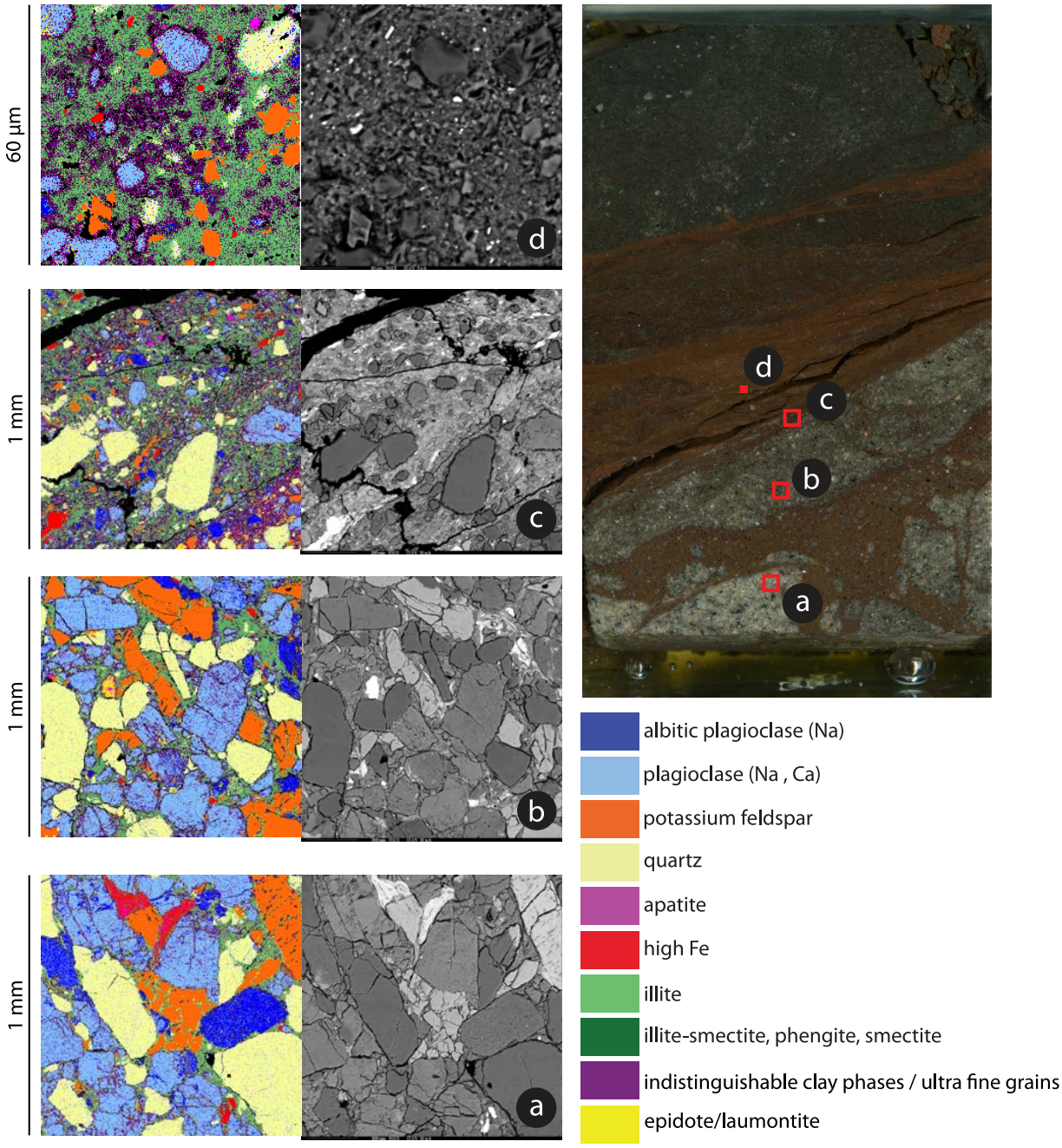

Figure 12: Images and Composite X-Ray Maps – Transect 1. BSE and composite X-ray map transect from the sandstone side of the fault in block 3067_3 from the cataclastic sandstone into the red-brown gouge showing increasing deformation with increasing strain.

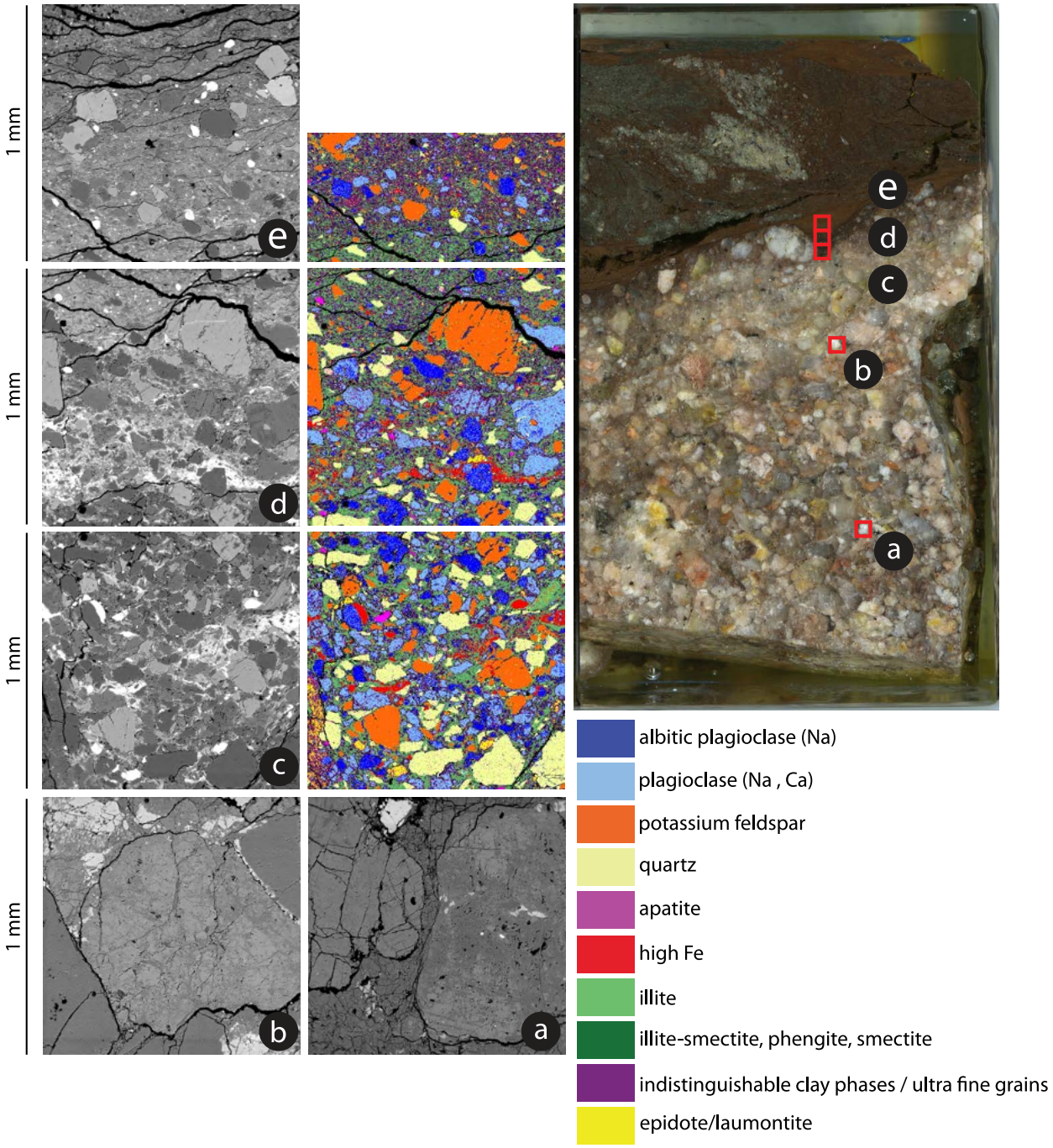

Figure 13: Images and Composite X-Ray Maps – Transect 2. BSE and composite X-ray maps from the host arkose unit, moving from less-deformed material away from the fault into the contact between the host arkose and brown gouge zone. X-ray maps were not created in the host arkose due to the large grain size with respect to the image size.

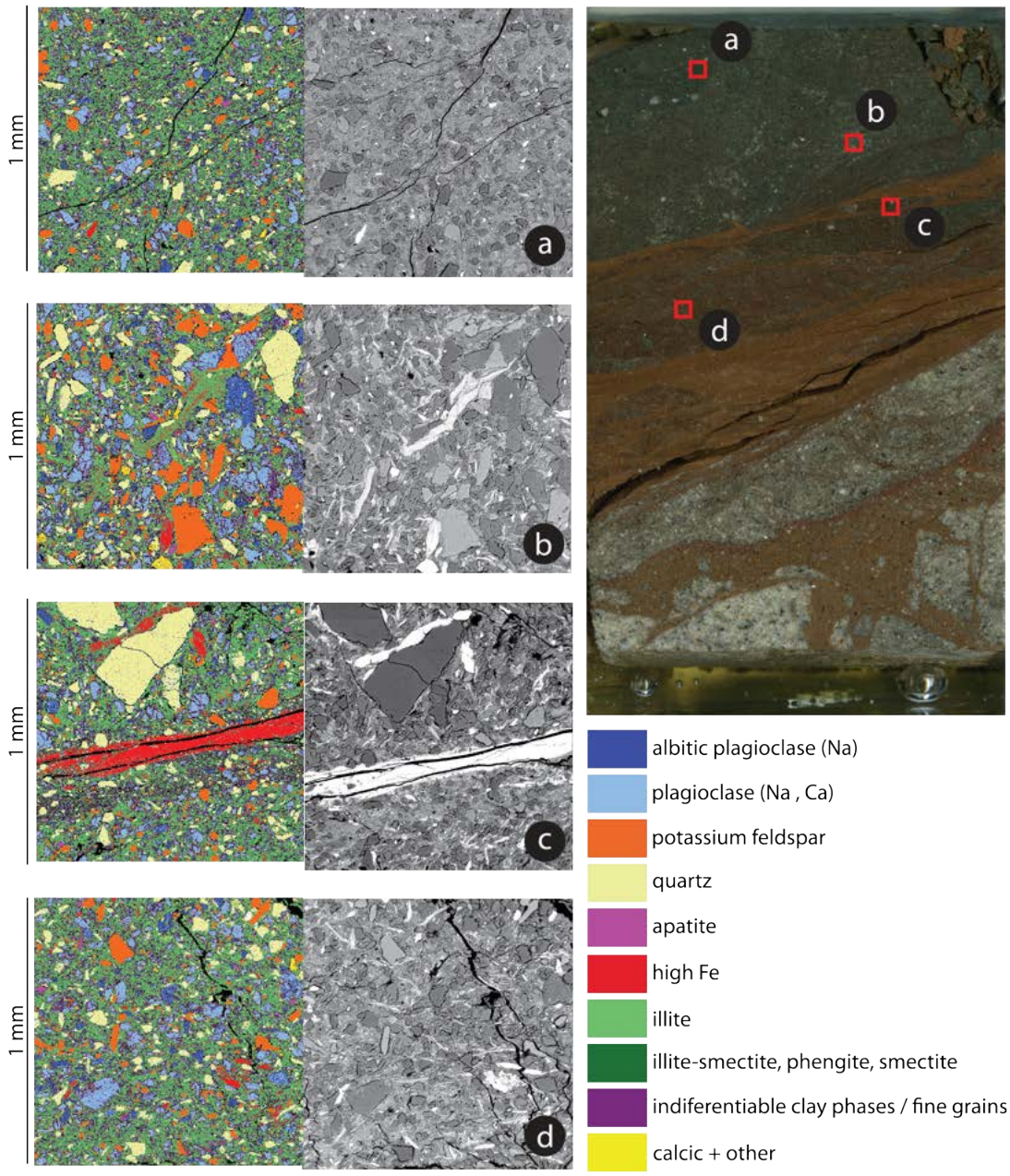

Figure 14: Images and Composite X-Ray Maps – Transect 3. BSE and composite X-ray map transect from the siltstone side of the fault in block 3067_3 from the host siltstone into the cataclastic sandstone.

The fine-grained matrix of the cSS zone (cSS(m)) contains 9.0% quartz, 8.0% albitic plagioclase, 17.5% other plagioclase, 10.2% orthoclase, 22.6% clay phases, and 26.2% indistinguishable phases. The cSS(m) contains grains as large as within the sandstone clasts, but has an average grain size of 53 μm (Table 4**)**, a greater population of smaller grains, and the percentage of clay phases and indistinguishable particles is twice that of the cSS unit (Tables 2 and 3**)**. Grains are blocky and do not show a major change in morphology compared to the cSS clasts. This is consistent with the lack of foliation within the cSS(m). Minor amounts of laumontite were found in the cSS(m) unit (Figure 12), but no other laumontite is found in the fault zone. Previous studies of the 3067 m MD fault report no laumontite (Solum et al., 2006). The laumontite is present within the matrix material (cSS(m)), rather than as fracture fill as seen in the HAS. Extensive observation within the matrix material was performed before any laumontite was encountered. While XRF images of the region are not capable of distinguishing laumontite from calcium bearing clay phases or very fine grained calcic plagioclase, the matrix region of the cSS is calcium rich compared to other units of the fault and compared to the sandstone clasts of the cSS zone.

The RBG contains 0.8% quartz, 2. 9% albitic plagioclase, 5.9% other plagioclase, 9.1% orthoclase, 36.9% clay phases, and 42.2% indistinguishable phases (Tables 2 and 3). The RBG analyses are performed primarily at the boundary with the cSS (Figure 12) to capture the transition to one of the finest grained zones in the fault and also for comparison to the increase in deformation documented by Heron (2011). This zone is composed of very fine-grained matrix material with elongate clasts of cSS and discrete

survivor grains. XRF scans show a sharp drop in calcium and silicon content, and a sharp increase in iron and potassium at this boundary. Average grain size determined from the 1 mm x 1 mm BSE images is 13 μm within the RBG material and 26 μm including the cSS clasts (Table 4). There are narrow zones of very fined grained material within the RBG. BSE and SE images were taken of this region at higher magnifications to investigate grain size beyond the resolution of the BSE images captured on the microprobe. Average grain size of the survivor particles at this scale is 0.71 μm (Table 4) and particles appear suspended in an indistinguishable matrix. Survivor grains within the RBG are more rounded than those in the cSS.

The cataclastic siltstone unit contains 6.2% quartz, 5.4% albitic plagioclase, 9.4% other plagioclase, 3.7% orthoclase, 39.5% clay phases, and 29.4% indistinguishable phases (Tables 2 and 3). Several the X-ray composite images capture portions of host siltstone clasts and regions of fine-grained material. These images are plotted separately as the cSlt/Slt unit and contain 6.4% quartz, 6.5% albitic plagioclase, 14.5% other plagioclase, 6.1% orthoclase, 34% clay phases and 29.9% indistinguishable phases. The host siltstone data is represented by composite X-ray maps that do not contain any of the fine-grained material present in the cSlt. The siltstone is composed of 5.9% quartz, 6.1% albitic plagioclase, 10.9% other plagioclase, 7.2% orthoclase, 38.4% clay phases and 27.4% indistinguishable phases. The transition from the RBG to the cSlt zone is not easily distinguishable in XRF images and shows only a minor increase in calcium and silicon, and a slight reduction in iron. Average grain sized within the cataclastic siltstone is 25 μm with angular grains showing pitting and phase contrasts within grains. The fine-

grained material bounding the grains contains numerous elongate particles with higher BSE signature than previously observed grains. These were investigated using EDS on the SEM and are composed of interlayered iron oxide and illitic clay phases. These are found throughout the siltstone and cataclastic siltstone units but are not observed in other structural units. The fine-grained regions of the cataclastic siltstone are similar to the RBG showing predominantly indistinguishable fine-grained material containing rounded survivor grains of various phases. The fine-grained material in the siltstone has regions of concentrated iron oxide, often in shear-zone-parallel bands. These are also found in the RBG but are less pronounced.

The brown gouge zone is 0.9% quartz, 5.2% albitic plagioclase, 2.9% other plagioclase, 3.7% orthoclase, 34.2% clay phases and 48.0% indistinguishable phases (Tables 2 and 3). The average mineralogy for all images is 7.2% quartz, 6.3% albitic plagioclase, 11.7% other plagioclase, 7.2% orthoclase, 31.1% clay phases, and 31.6% indistinguishable phases. The average grain size of survivor particles is 29 μm (Table 4**)**. The fine-grained material is very similar in appearance to the finest-grained zones of the RBG and contains rounded survivor grains within a foliated fine-grained matrix. Feldspar and quartz phases decrease systematically towards the shear zones while clay phases and indistinguishable phases increase representing an increase in clay phases within zones of greater alteration as well an increase in particles below the resolvable particle size.

WDS data from each BSE image location are reported in Appendix 1. Composition of feldspar grains shows a range of values, but the range of compositions is consistent

across all structural domains. Plagioclase grains range from nearly pure albite up to andesine in composition with a maximum anorthite composition of An_{40}. Orthoclase grains are all Or_{85} or greater. Some grains show a minor, but statistically significant celsian component up to 5.0% (Appendix 1). Pitted feldspar grains area found in all structural units and in several cases clay phases were found crystallized within the feldspar pits. EDS analysis showed these to be illitic clays.

5.3 Grain Size and Shear Localization

A robust grain size analysis was not part of this study. Approximate grain size measurements were made within each identified fault rock zone in order to compare fault rocks from this study to those of earlier studies. The work of Heron et al., 2011 studied grain size and comminution mechanism in detail on samples taken nearby to the 3067 m MD fault. Generalized grain size analysis of the structural domains of the 3067 m MD fault is used to place each domain into the context of the Heron et al. study and relative average grain size across structural domains of the 3067 m MD fault is used as a proxy for deformation of each zone. Average, maximum, and minimum observable grain size are reported in Table 4**.** Investigation of relative grain size was also used to approximate shear zone widths. Several bands of ultra-fine grained material were identified as potential shear zones with an average width of ~0.0005 m. The widest portion of the RGB zone is ~0.01 m wide and is used as the upper limit of shear zone width in the shear heating models.

5.4 Vitrinite Reflectance

Vitrinite reflectance data are reported for three zones within the 3067_1 block (Figure 4). The zones a, b, c in Figure 4 correspond to the cataclastic siltstone (cSlt), red-brown gouge (RBG), and host siltstone (Slt). Mean reflectance (%Ro) is 1.59% for zone a, with n = 43, 1.50% for zone b with n=11, and 1.65% for zone c with n = 160. The wide range in n values is due to the scarcity of vitrinite particles outside of the siltstone. There are very few particles within the RBG and of those encountered most were a few microns in diameter. Measurements require that the particles have several smooth surfaces at least 0.1 micron in size and the few particles encountered in the RGB were too small to be measured reliably. Zone c has the highest mean value, but the modal bins of each histogram are in the same range at approximately 1.5%Ro.

The population of reflectance values measured in blocks 3067_3 and 3067_6 are reported in Figure 5. Locations of each measured particle are plotted on the blocks and the mean reflectance values and n-values are report in the histograms. Mean %Ro for block 3067_3 is 1.86% with n = 301 and 1.96% for block 3067_6 with n = 50. The difference in n values is again due to the limited number of vitrinite and measurable vitrinite in the sample

Block 3067_3 contains portions of all major structural units with the exception of the host arkose and block 3067_6 contains a zone in which siltstone clasts containing vitrinite are in close proximity to the BG. These blocks were selected for analysis to determine reflectance values for each zone, and to increase the likelihood of measuring reflectance values in close proximity to shear zones.

All blocks were explored for the distribution of vitrinite. Vitrinite was only found in the host siltstone, cataclastic siltstone, red-brown gouge and brown gouge zones. The host siltstone contains ample vitrinite particles large enough for analysis. Vitrinite present in the cataclastic siltstone and red-brown gouge was predominantly found within clasts of intact siltstone. Few discreet vitrinite particles were found within the red-brown gouge and brown gouge zones.

The highest mean reflectance values were found in the siltstone samples collected above the 3067 m MD fault in the SAFOD core. Sample locations for each of the siltstone chips along with their mean reflectance values are shown in Figure 15. Sample P1B23-2a has a mean reflectance of 2.07%, mean reflectance of sample P1B22-1a is 2.09%, and sample P1B21-1 has a mean reflectance is 1.94% yielding a mean reflectance of 2.03% for the siltstone chips.

Data from Kirschner et al. (2006) report reflectance data from samples in the Phase 2 core at depths from 2565 to 2973 m TVD (Figure 16). Data were reported by two different petrographers and show significant spread (up to ~1.0%) but good agreement below ~2600 m TVD. The mean values increase with depth from ~0.70% to 0.95% (Figure 16).

The Easy%Ro model predicts reflectance values of ~0.6% at the true vertical depth of the 3067 m MD depth fault (2558 m TVD) using conservative estimates of geothermal gradient and a wide range of ages from published age constraints (e.g. Schleicher et al., 2010; Springer et al., 2009; Williams, 2004). Geothermal gradient, and subsequently maximum temperature, are the greatest controls on modeled

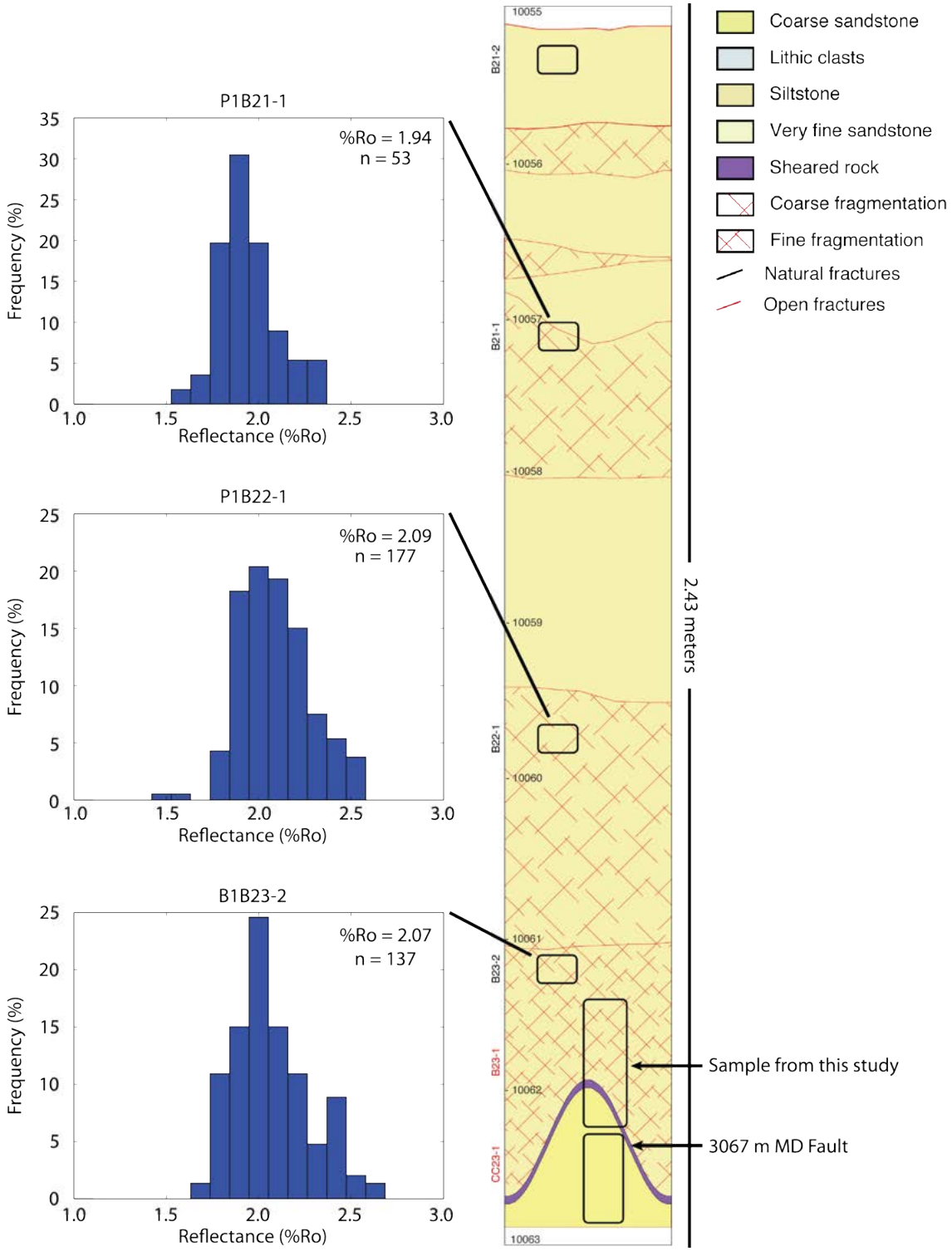

Figure 15: Sample Locations and Vitrinite Reflectance Populations of Siltstone Samples. Portion of phase 1 core map with the sample locations of the 3067 m MD fault and the three siltstone chips from this study. Histograms show reflectance values for each siltstone sample along with mean reflectance and n-values. The phase 1 core map is modified from Almeida (2007).

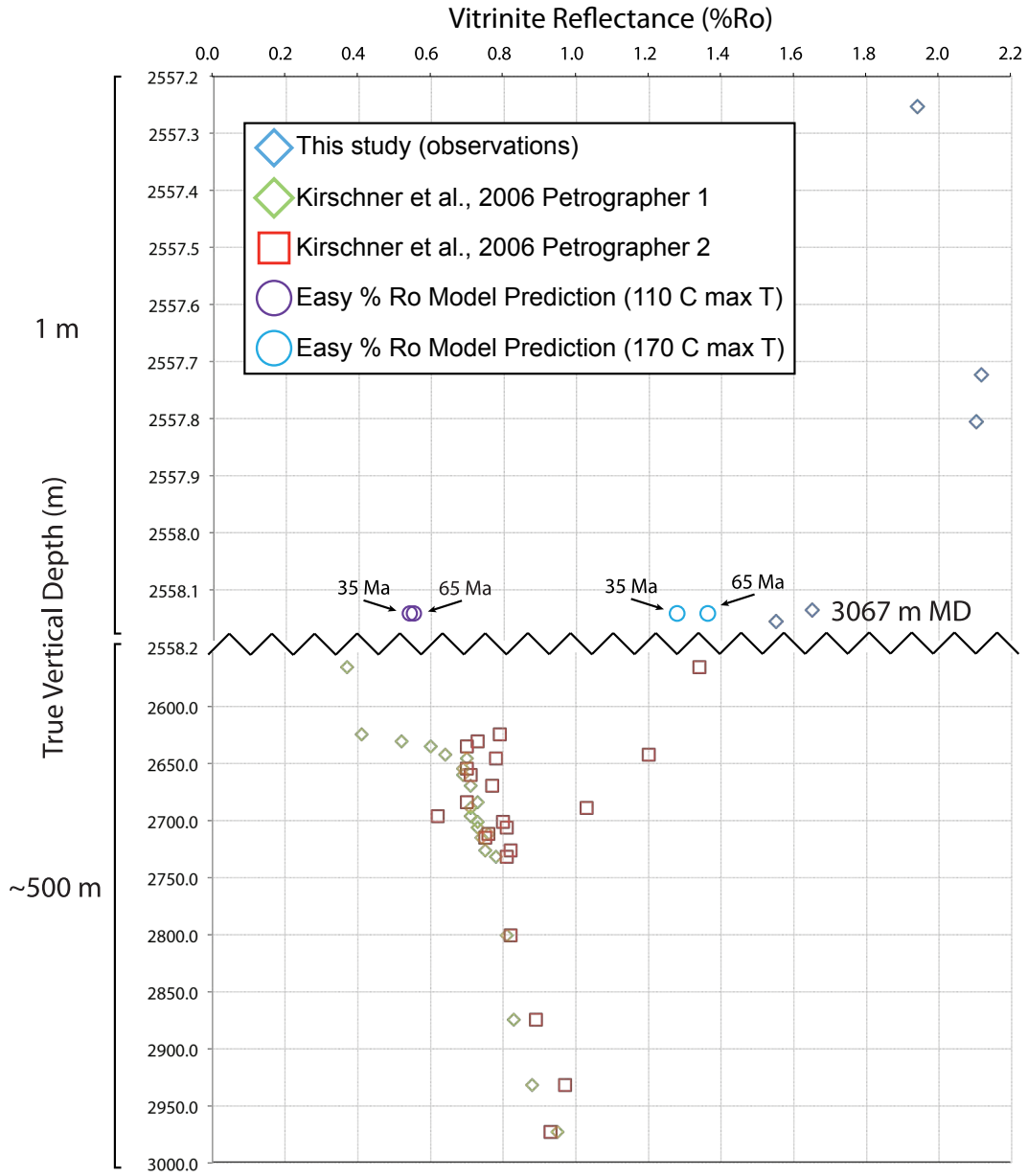

Figure 16: Consolidated Vitrinite Reflectance and Modeled Maturity Data. Plot of vitrinite reflectance (%Ro) versus true vertical depth in meters for data from this study, values from Kirschner et al. (2006) measured from phase 2 samples, and predicted reflectance values from the Easy%Ro model for the 3067 m MD fault. Note the change in vertical scale.

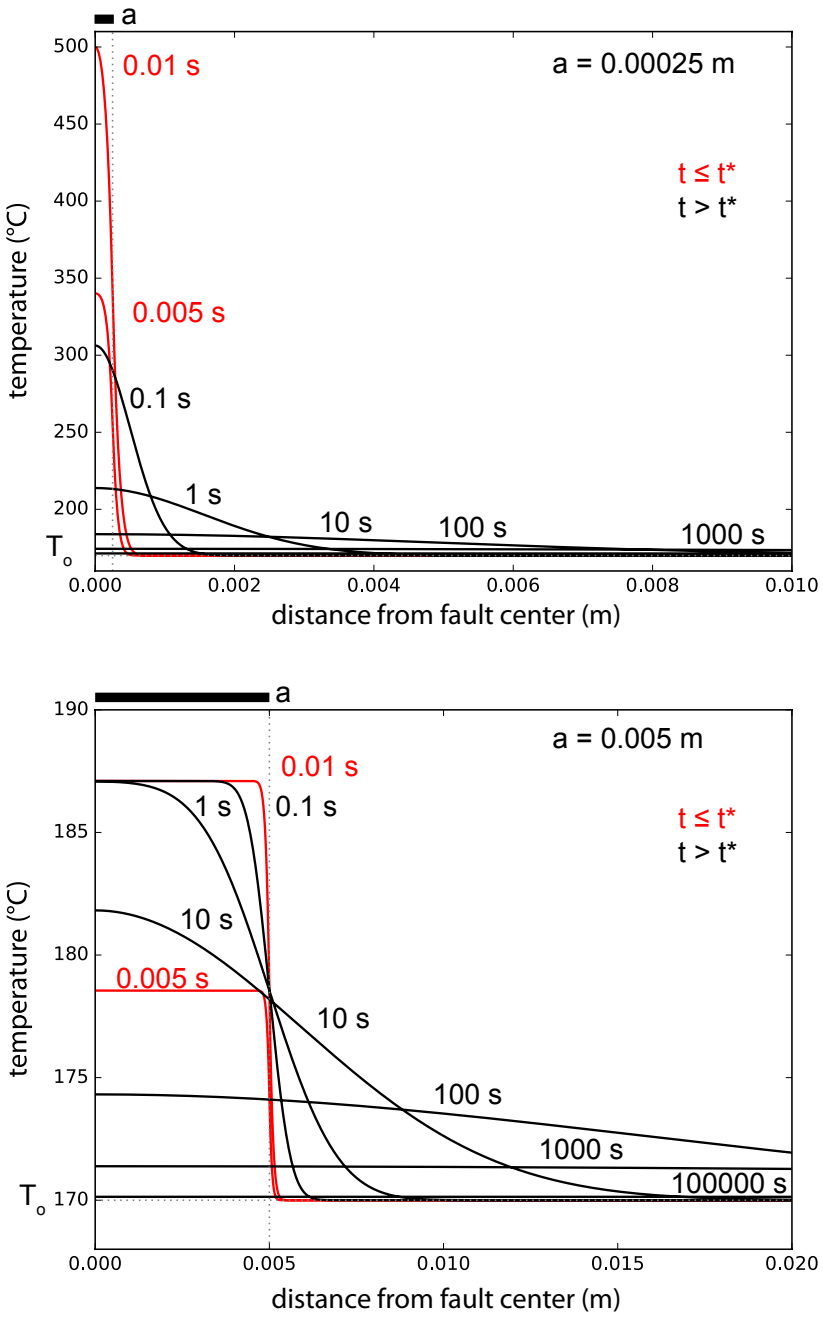

Figure 17: Modeled Heat Generation for Narrow and Wide Faults. Modeling results of temperature as a function of distance from fault center at various time steps after fault slip initiation for a narrow shear zone (top) and wide fault zone (bottom). Red curves represent temperature profiles during slip.

reflectance from burial. Figure 16 shows modeled vitrinite reflectance assuming ages from 35 to 65 MA at both present day in-situ temperature of 110 °C and maximum burial temperature of 170 °C. The difference in reflectance from the age of the sediment is negligible in the 110 °C case and approximately 0.1 percentage point difference at 170 °C. Both of these modeled reflectance values from burial are below the observed mean reflectance values from both blocks of the 3067 m MD fault, and from the three siltstone blocks above the 3067 m MD fault (Figure 16).

5.5 Numerical Modeling of Shear Heating and Vitrinite Response

Published values for stress magnitude, thermal rock properties, and mechanical properties of the fault rock are the basis for the numerical modeling of shear heating and vitrinite response in this study. Hickman et al. (2004) established an empirical relationship between depth and horizontal stress orientations as well as horizontal and vertical stress magnitudes. The work by Hickman et al. (2004) define the magnitude of the stress tensor used in this modeling work. Principal stress orientations determined by Almeida et al. (2007) are in general agreement with those of Hickman, et al. (2004) suggesting that present day stresses are similar to those at the time of fault formation (Figures 7, 8). The stress orientations established by Almeida et al. (2007) are chosen as the basis for this modeling work, and are chosen over those of Hickman et al. (2004) because the Almeida et al. (2007) work established orientation estimates in three dimensions instead of only horizontal maximum and minimum stress.

Resolving these values on to the possible orientations of the 3067 m MD fault yields the shear and normal stress magnitudes across several possible orientations. Values for

shear and normal stress as a function of orientation with respect to the SAFOD borehole are show in Figure 9**.** Values for shear failure assuming Byerlee (1978) friction of μ = 0.6 and for the experimentally derived value of μ = 0.4 determined by Kitajima et al. (2011) are plotted showing orientation-dependent changes in proximity to failure. All stress values are effective stress and assume a normal hydrostatic gradient. Stress magnitudes are modeled for present day TVD of 2558 m and maximum inferred TVD of 4236 m. Four possible fault plane orientations representing two conjugate orientations produce shear stress across the fault plane which reaches the failure threshold assuming μ = 0.4 (Figure 9). At each of these four possible failure orientations, the local maxima for shear and normal stress are similar, and given uncertainty about the true orientation, average values of 85 and 34 MPa are used for normal stress and shear stress during faulting.

Shear heating models for a 0.01 m slip event, with shear zone thicknesses of 0.0005 and 0.01 m are modeled to constrain the magnitude of temperatures within and away from the fault zone at various time steps during and after faulting following the work of Fulton et al. (2012; Figure 17). These spatiotemporal temperature profiles are the inputs for the Easy %Ro model that is then used to predict the subsequent vitrinite maturation response. A full list of model parameters is shown in Table 1.

Models are produced for the thin fault and thick fault scenarios for displacements from 0.01 m to 0.05 m. The temperature vs. time profile is modeled for different distances away from the shear zone center both within and away from the shear zone (Figures 18, 19).

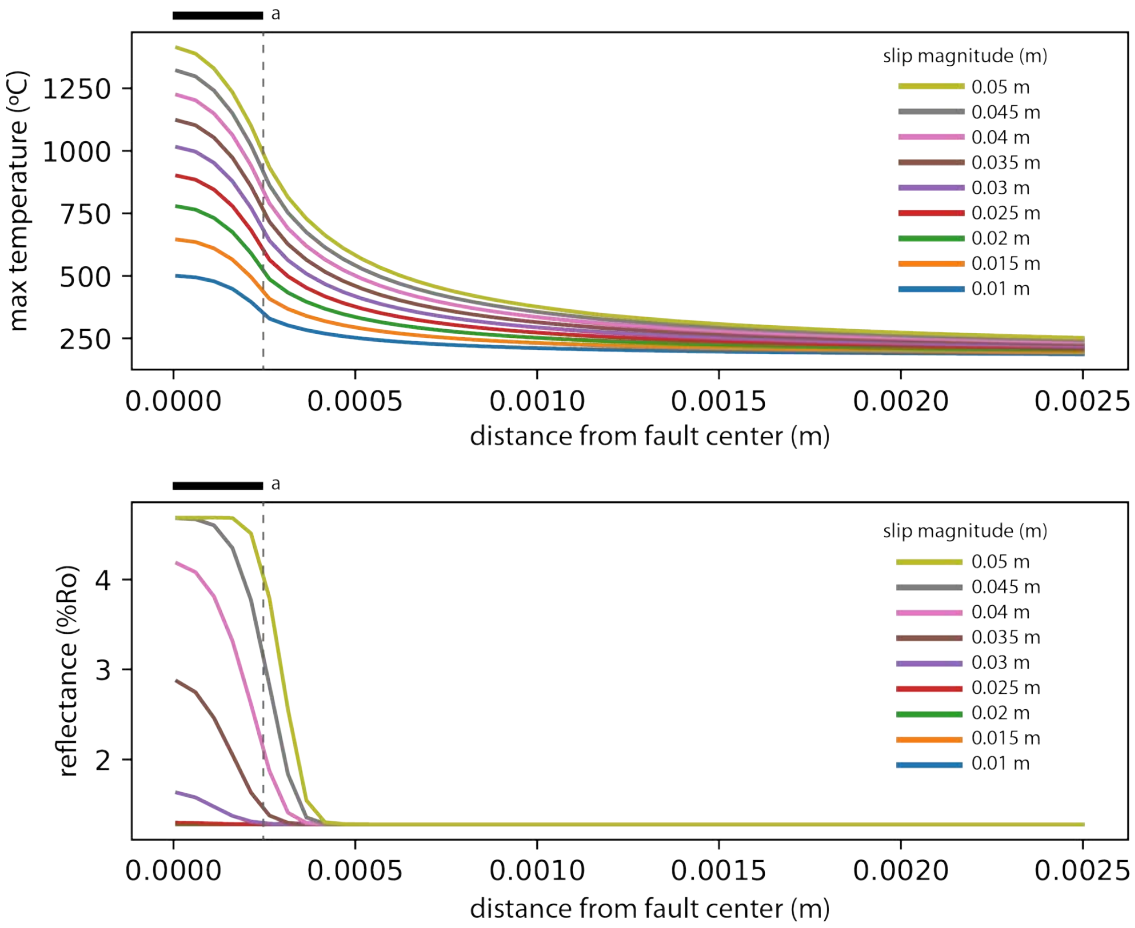

Figure 18: Modeled Frictional Heating and Vitrinite Response, Narrow Fault. Modeled maximum temperature from faulting as a function of distance from shear zone center (top) and the resulting modeled vitrinite reflectance response (bottom) for a narrow shear zone.

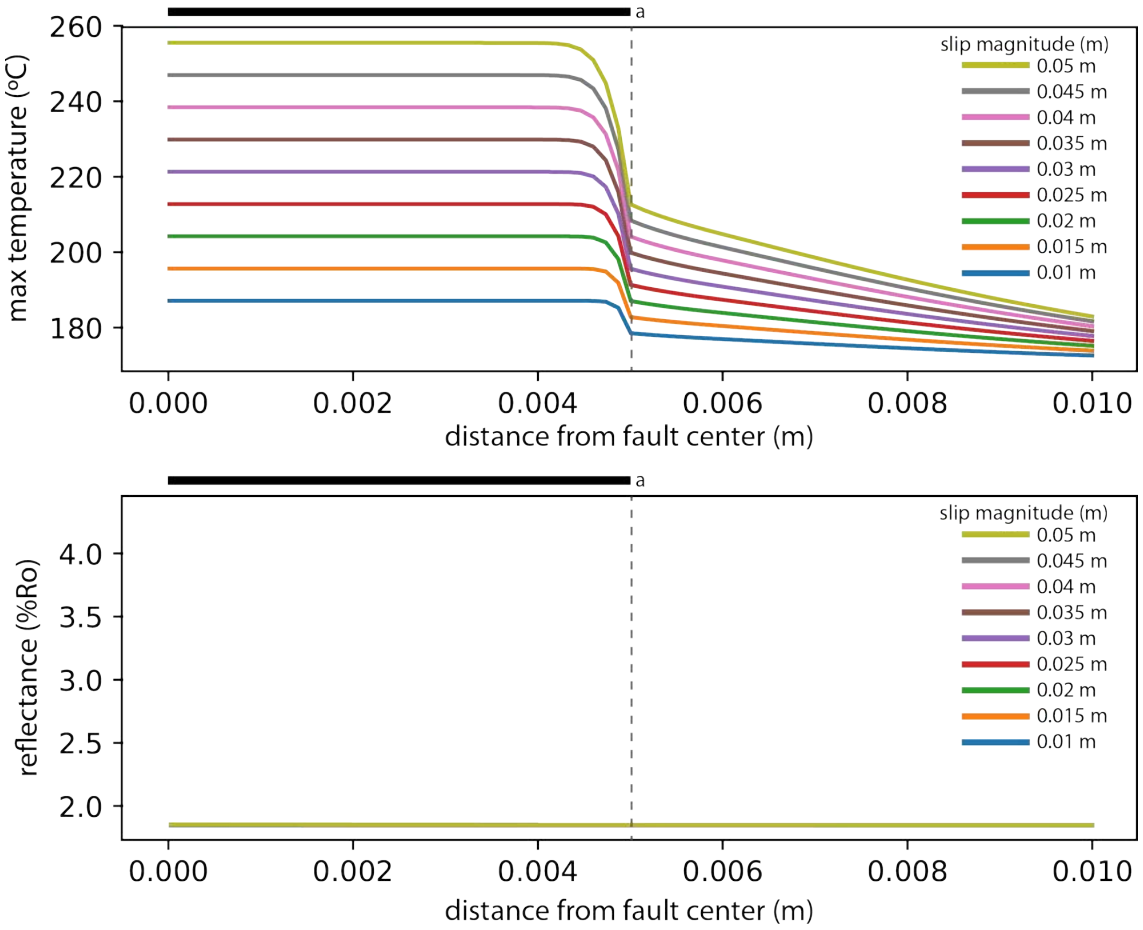

Figure 19: Modeled Frictional Heating and Vitrinite Response, Wide Fault. Modeled maximum temperature from faulting as a function of distance from shear zone center (top) and the resulting modeled vitrinite reflectance response (bottom) for a wide shear zone.

For the narrow fault scenario, maximum temperature from heating ranges from 500 °C for a 0.01 m slip event to over 1400 °C for a 0.05 m slip event. In this narrow fault scenario, a slip event of 0.03 m produces a maximum temperature at in the shear zone center of 1014 °C resulting in a %Ro value of 1.63%. All modeled slip magnitudes below 0.03 m do not produce an observable %Ro increase, and for the 0.03 m slip event, elevated %Ro values are confined to within the 0.005 m shear zone. At slip magnitudes of 0.035 m and above diffusion of heat produces high enough temperatures to produce increased %Ro values outside of the shear zone up to a maximum distance of approximately twice the shear zone thickness for a slip magnitude of 0.05 m. Slip events of 0.035 m and above produce maximum %Ro values from ~3.0% up to nearly 5% where values approach maximum possible reflectance values.

The wide fault scenario, for the same range of slip events from 0.01 to 0.05 m, produces maximum temperatures of 187 to 255 °C. Temperature distribution is uniform across the shear zone and drops off at the edge of shear zone where diffusion then becomes the source of increased hea.t None of the modeled slip magnitudes produce an increased vitrinite reflectance signature. Slip magnitudes between 0.25 m and 0.30 m are required with a 0.01 m wide shear zone to produce vitrinite reflectance values in the range observed across the 3067 m MD fault.

6. DISCUSSION

6.1 Structure and Mineralogy of Deformation

The 3067 m MD fault is larger than the faults studied by Heron (2011) but the structure and mineralogy that accompany deformation within the faults show similarities in host rock composition and likely comminution mechanism. The composition of the cataclastic sandstone unit is the closest analogue to the brecciated sandstones from Heron (2011) and the structural units share a similar composition of feldspars with the samples from Heron (2011) containing a greater initial orthoclase content. This study, and the work of Solum et al. (2006), Schleicher et al. (2009), and Kitajima et al. (2006) agree that the main alteration product within the 3067 m MD fault and the siltstones just above the fault are illite and illite-smectite clay phases. The dominant alteration product in the faults studied by Heron (2011) is laumontite, with illite present in minor quantities within the most highly deformed material. Comparison of BSE images from Heron (2011) and this study show similar signatures of feldspar alteration, grain size distribution, and matrix fill with the exception that the grains from Heron (2011) are bounded by laumontite rather than clay phases, and this study found minor only minor laumontite in the less-deformed host arkosic sandstone.

Albitization reactions release calcium ions into solution and both montmorillonite and laumontite are known to precipitate as a result (Boles, 1982; Ramseyer et al., 1992). The montmorillonite then alters to increasingly illitic interlayered illite-smectite with increasing burial and diagenesis (Hower et al., 1976) The albitization reaction is influence by the composition of formation fluid and the crystal structure of the initial

plagioclase, and is enhanced by fracture (Ramseyer et al., 1992). Differences fluid chemistry, potentially related to fluid compartmentalization by the 3067 m MD fault, may have influenced the albitization reaction. Detailed composition of the plagioclase is not available from Heron (2011), and this too may have influenced the production of laumontite rather than clays. The presence of the siltstone juxtaposed against the arkosic sandstone within the 3067 m MD fault may have influenced the pore fluid chemistry as well.

The lack of well constrained timing of the formation of these damage zone faults implies that the 3067 m MD fault and the faults studied by Heron (2011) may have formed more than 30 million years apart under vastly different conditions with respect to fluid chemistry and thermal regime. This is supported by the clay mineralogy documented by Schleicher et al. (2009b) which presents evidence for illite and illite-smectite present within the same material but with mineralogical indicators suggesting different temperature and fluid conditions at the time of crystallization.

The progression from the host arkosic sandstone to the RBG and BG zones is structurally similar to the smaller faults studied by Heron (2011). The fabric within the finest grain material shows evidence of shear with particle size reduction to the nanometer scale and rounding of survivor grains within the finest grained material. This particle size reduction is accompanied by alteration of feldspar to illite and illite smectite and the specific portions of clay phases and indistinguishable phases reported in this study agree with published data of clay mineralogy from the fault.

6.2 Thermal History, Vitrinite Reflectance, and Modeling of Shear Heating and Maturation of Organic Material

The observation of anomalously high reflectance values within fault zones is a well-documented phenomenon (Taylor et al., 1998), but one that lacks a definitive explanation (Bustin, 1983; Fulton & Harris, 2012; Kitamura et al., 2012). The relatively sparse population of organic particles within the 3067 m MD fault is an added challenge in this study. There are, however, numerous particles comprising a population with a mean reflectance greater than that predicted from burial alone. In the absence of an obvious mechanism for the anomalously high values observed in fault zones several possible explanations are commonly proposed. Dilatant behavior within fault zones may accommodate transient fluid flow from greater depths resulting in high-temperature pore fluids migrating through the shear zone. There is not, however, compelling data in form of anomalous mineralization to support this. In the case of the 3067 m MD fault it is possible that the fault zone nucleated in a depositional interval containing organic material previously matured by mechanisms other than in-situ burial. The meso-scale mapping of this shear zone by Almeida, et al. (2005, 2007) regional structural trends, and modeling of this study suggest the most likely orientation of the 3067 m MD fault to be sub-vertical, making a stratigraphic origin less likely, though a sub-horizontal orientation could be supported by modeling alone. Another possible explanation is that accepted models of vitrinite reflectance are not sufficient for explaining maturation of organics on short time scales as expected from shear heating.

In the 3067 m MD fault specifically, The ~2 m of siltstone above the shear zone including the host siltstone of the 3067 m fault show anomalously high vitrinite reflectance values compared with results from Easy%Ro modeling and with values from phase 2 samples deeper in the borehole **(**Figure 16**).** This observation is consistent with other observations of anomalous reflectance observations in shear zones. Draper-Springer, et al., provide a constraint on maximum burial temperature of 170° C, which would result in reflectance values from burial of ~1.3%. The high reflectance values span a distance of at least 1 m, with highest values found in the siltstone samples 0.3 and 0.6 m above the 3067 m MD fault. This is not well explained even by a single large event or even multiple large events as a shear zone of this thickness would require an unrealistically large slip event to produce the observed reflectance values.

Modeling of shear heating shows that maturation of a few tenths of a percent above background due to burial, as needed to explain the observations of this study, is possible with slip events of ~3 cm given a 0.5 mm wide shear zone. The magnitude of slip necessary to produce these results decreases with decreasing shear zone width. The distribution of reflectance values in the organic-bearing zones of the 3067 m MD fault and the siltstone samples above the fault can be explained by diffuse, small-scale slip events on a very large number of shear surfaces. It is possible to imagine a scenario in which deformation at inception of slip is distributed across a zone a few meters thick, especially in a lithology with lower shear strength. The siltstone of the 3067 m MD fault and rock above it may be influencing such behavior. Numerous small scale slip events, potentially millimeters or less across shear zones approaching single grain diameters in

thickness could produce a distribution of heating and maturation similar to that observed in the siltstone and shear zone of the 3067 m md fault. This concept, coupled with any sort of shear-strengthening behavior may provide a viable explanation for distribution of anomalously high vitrinite maturation values across such a large zone.

Fulton and Harris, 2012, using Easy%Ro modeling, demonstrate that reflectance is controlled by maximum temperature largely insensitive to the number of events. Zones such as the 2067 m MD fault, therefore, may have experienced greater strain, but should not necessarily show greater reflectance values if the strain occurred under a different stress regime, at different slip rates, in a different thermal regime, or across a broader shear zone. Additionally, elevated reflectance values are confined almost exclusively to within the shear zone at the scale of events modeled in this study suggesting that elevated reflectance values across a shear zone necessitates distributed shear to explain distributed high reflectance values. The extent to which this behavior is lithologically controlled or controlled by the degree of fault maturity is another question.

This ultimately brings into question the assumptions of the constitutive equations used in such modeling. Models of shear heating assume simultaneous, distributed shear within half-width of the shear zone during slip. While modeling shows that no recordable organic maturation would result from a 5 cm slip event on a 1 cm shear zone, if shear in that zone were accommodated simultaneously on 20 discrete 0.5 mm shear zones, a slip event of 3 cm would result in observable maturation and a 5 cm event would mature organics to maximum reflectivity. Given that organics within shear zone are more mature than background, but non-uniformly, the idea of non-uniform

spatiotemporal slip distribution could explain the non-uniform distribution of organic maturation.

7. SUMMARY

Mineralogy of the bounding arkosic sandstone is similar in composition to that of the arkosic sandstone studied by Heron, et al. (2011) but the siltstone units show a different composition. The presence of organics exclusively in the siltstone, and localization of shear in the siltstone units suggests a lithologic influence on the 3067 m MD fault and potentially different deformation styles and mechanisms.

Increased vitrinite reflectance values within the 3067 m MD fault can be explained by shear heating from displacements on the order of millimeters to centimeters or less with narrow shear zones. Modeling of slip at in-situ conditions suggests shear heating and maturation is a viable explanation for the observed reflectance values.

Modeling of slip and heating is in agreement with the likely sub-vertical fault orientation suggested by Almeida et al. (2005, 2007) and is consistent with the values of frictional coefficient determined by Kitajima et al. (2009). At both the present day and inferred historical maximum TVD the failure envelope is only reached assuming the frictional coefficient deteremed by Kitajima et al. At the inferred historical maximum TVD of 4236 m, failure is only reached in these preferred orientations, which supports the maximum inferred maximum burial depths. For deeper burial depths a lower frictional coefficient would be required to initiate slip.

A single zone of consistently high reflectance values is not seen within the 3067 m MD with the exception of the foliated brown gouge (BG), though due to the very fine grain size of this zone, only two measurements were made. This is consistent with modeling results, which show that for events on the order of mm to a few cm, any

anomalous heating signature would be found only within the shear zone. Distribution of high reflectance values is sporadic across the shear zone, which is reasonable based on modeling results

Observable increases in reflectance values at the background maturity level of the 3067 m MD fault require maximum temperatures of ~1000° C which is possible as demonstrated by the modeling portion of this work.

Likely orientation of the 3067 m md fault is sub-vertical, supported by modeling of stress across possible fault plane orientations determined by Almeida et al. (2005) and the experimentally derived failure criterion of Kitajima et al. (2009).

Vitrinite reflectance values across the 3067 m MD and in the deformed shale above the fault are higher than predicted by models of burial alone and higher than observed valued slightly deeper in the SAFOD borehole. This is consistent with long-standing observations of increased vitrinite reflectance values in shear zones.

Modeling of shear heating and subsequent maturation shows that shear heating from faulting would only produce elevated vitrinite values for particles within or immediately adjacent to shear zones which is consistent with the heterogeneity of observed reflectance values within the fault. Homogenous reflectance values across the shear zone would require either much greater slip magnitudes or a nearly perfect distribution of equal magnitude small slip events across the shear zone.

The extrapolated stress observations of Hickman et al. (2004) are in agreement with the stress orientations inferred by Almeida et al. (2005) and result in values of shear and

normal stress across a sub-vertical fault orientation which would produce failure conditions.

8. CONCLUSIONS

1. The 3067 m MD fault displays significant localization of slip and comminution, which is consistent with seismic slip but not unique to seismic slip.

2. The fault rocks display records of water and mineral alteration reactions associated with comminution and faulting.

3. Vitrinite reflectance data from this study, combined with other measurements of reflectance in previous studies, demonstrate a change in reflectance across the 3067 m MD fault consistent with relatively large cumulative slip and juxtaposition of different rock units with different thermal histories.

4. Although the vitrinite data do not provide a definitive signature of a significant temperature increase as evidence of seismic slip in the final preserved localized zones of the 3067 m MD fault, there is evidence of scattered comminuted particles within the fault that show high vitrinite reflectance. These scattered, high-vitrinite-reflectance particles could reflect some localized seismic heating, possibly during earlier stages of faulting that were disrupted by subsequent faulting events.

REFERENCES

Allmendinger, R. and Cardozo, N., 2013. *Stereonet*. Version 9.2.3. http://www.geo.cornell.edu/geology/faculty/RWA/programs/stereonet.html

Almeida, R. V. (2007). Mesoscale fracture fabric and paleostress along the San Andreas fault at SAFOD. (Master's Thesis) Texas A&M University, College Station, TX, 90 pgs.

Almeida, R., Chester, J.S., Chester, F.M. (2007) Similarity of paleostress and in situ stress at SAFOD and implications for a weak San Andreas Fault, EarthScope National Meeting, Monterey, CA, March 27-30.

Almeida, R., Chester, J.S., Chester, F.M., Kirschner, D.L., Waller, T. D., Moore, D.E. (2005). Mesoscale structure and lithology of the SAFOD Phase I and II core samples, *EOS Trans. AGU*, T21A-0454, 86(52).

Ben-Zion, Y., & Sammis, C. G. (2013). Shear heating during distributed fracturing and pulverization of rocks. *Geology*, *41*(2), 139–142. https://doi.org/10.1130/G33665.1

Billi, A. (2005). Grain size distribution and thickness of breccia and gouge zones from thin (<1m) strike-slip fault cores in limestone. *Journal of Structural Geology*, 27(10), 1823 - 1837. https://doi.org/10.1016/j.jsg.2005.05.013

Boles, J. R. (1982). Active albitization of plagioclase, gulf coast Tertiary. *American Journal of Science*, *282*(2), 165–180. https://doi.org/10.2475/ajs.282.2.165

Burnham, A. K., & Sweeney, J. J. (1989). A chemical kinetic model of vitrinite maturation and reflectance. *Geochimica Et Cosmochimica Acta*, *53*(10), 2649–2657. https://doi.org/10.1016/0016-7037(89)90136-1

Bustin, R. M. (1983). Heating during thrust faulting in the rocky mountains: friction or fiction? *Tectonophysics*, *95*(3-4), 309–328. https://doi.org/10.1016/0040-1951(83)90075-6

Byerlee, J. (1978). Friction of rocks. *Pure and Applied Geophysics*, *116*(4), 615–626. https://doi.org/10.1007/BF00876528

Chester, F. M., & Chester, J. S. (1998). Ultracataclasite structure and friction processes of the Punchbowl fault, San Andreas system, California. *Tectonophysics*, *295*(1-2), 199–221. https://doi.org/10.1016/S0040-1951(98)00121-8

Chester, F., Evans, J., & Biegel, R. (1993). Internal Structure and Weakening Mechanisms of the San-Andreas Fault. *Journal of Geophysical Research; Solid*

Earth, *98*, 771–786. https://doi.org/10.1029/92JB01866

Chester, J.S. & Chester, F.M. (2006). Energy Dissipation and Damage Generation in Seismic Fault Zones, *Eos Trans. AGU*, 87(52), T43A-1632.

Chester, J.S., Chester, F., Almeida, R. Kitajima, H., Shimamoto, T., Evans, J. & Kirschner, D. (2006). Slip localization, damage, and dynamic weakening of large displacement faults of the San Andreas System, *6th Joint Meeting of the UJNR Panel on Earthquake Research*, Tokushima, Japan, Technical session: Mechanisms, p. 036.

Chester, J. S., Chester, F. M., & Kronenberg, A. K. (2005). Fracture surface energy of the Punchbowl fault, San Andreas system. *Nature*, *437*(7055), 133–136. https://doi.org/10.1038/nature03942.

Cowan, D. S. (1999). Do faults preserve a record of seismic slip? A field geologist's opinion. *Journal of Structural Geology*, *21*(8), 995–1001. https://doi.org/10.1016/S0191-8141(99)00046-2

Eppelbaum, L., Kutasov, I., & Pilchin, A. (2014). Thermal Properties of Rocks and Density of Fluids. *Lecture Notes in Earth System Sciences* (pp. 99–149). Berlin, Heidelberg: Springer Berlin Heidelberg. https://doi.org/10.1007/978-3-642-34023-9_2

Evans, J. P., & Chester, F. M. (1995). Fluid-rock interaction in faults of the San Andreas system: Inferences from San Gabriel fault rock geochemistry and microstructures. *J Geophys Res*, *100*(B7), 13007. https://doi.org/10.1029/94JB02625

Fulton, P. M., & Harris, R. N. (2012). Thermal considerations in inferring frictional heating from vitrinite reflectance and implications for shallow coseismic slip within the Nankai Subduction Zone. *Earth and Planetary Science Letters*. https://doi.org/10.1016/j.epsl.2012.04.012

Graham, S. A., Stanley, R. G., Bent, J. V., & Carter, J. B. (1989). Oligocene and Miocene paleogeography of central California and displacement along the San Andreas fault. *Geological Society of America Bulletin*, *101*(5), 711–730. https://doi.org/10.1130/0016-7606(1989)101<0711:OAMPOC>2.3.CO;2

Grant, J. A. (2005). Isocon analysis: A brief review of the method and applications. *Physics and Chemistry of the Earth*. https://10.1016/j.pce.2004.11.003

Heron, B. (2011). *Grain-scale Comminution and Alteration of Arkosic Rocks in the Damage Zone of the San Andreas Fault at SAFOD.* (Master's Thesis). Texas A&M University, College Station, TX, 118 pgs.

Heron, B., Chester, J.S., Chester, F.M., Guillemette, R. (2011a). Densification and Alteration of Siliciclastics Adjacent to the San Andreas Fault at SAFOD: Implications for Seismic Velocity Structure and Fluid Flow, *AAPG Abstracts with Programs* #90124.

Heron, B., Chester, J.S., Guillemette, R., and Chester, F.M. (2011b). Comminution and Mineralization of Subsidiary Faults in the Damage Zone of the San Andreas Fault at SAFOD, *EarthScope National Meeting*, Austin, TX, May 18-20.

Hickman, S., & Zoback, M. (2004). Stress orientations and magnitudes in the SAFOD pilot hole. *Geophysical Research Letters*, *31*. https://doi.org/10.1029/2004GL020043

Hower, J., Eslinger, E. V., Hower, M. E., & Perry, E. A. (1976). Mechanism of burial metamorphism of argillaceous sediment: 1. Mineralogical and chemical evidence. GSA Bulletin ; 87 (5): 725–737. doi: https://doi.org/10.1130/0016-7606(1976)87<725:MOBMOA>2.0.CO;2

Kanamori, H., & Rivera, L. (2006). Energy partitioning during an earthquake. *Geophysical Monograph Series*, *170*, 3–13. https://doi.org/10.1029/170GM03

Keulen, N., Heilbronner, R., Stünitz, H., Boullier, A.-M., & Ito, H. (2007). Grain size distributions of fault rocks: A comparison between experimentally and naturally deformed granitoids. *Journal of Structural Geology*, *29*(8), 1282–1300. https://doi.org/10.1016/j.jsg.2007.04.003

Kitajima, H., J. S. Chester, F. M. Chester, and T. Shimamoto (2009). Characterization of frictional heating, mechanical behavior, and microstructure evolution of Punchbowl Fault ultracataclasite sheared at seismic slip rates: Implications for dynamic weakening mechanism, *Eos Trans. AGU*, 90(52), Fall Meet. Suppl., Abstract T41A-2002.

Kitamura, M., Mukoyoshi, H., Fulton, P. M., & Hirose, T. (2012). Coal maturation by frictional heat during rapid fault slip. *Geophys Res Lett*, *39*(16), L16302. https://doi.org/10.1029/2012GL052316

Lachenbruch, A. H. (1980). Frictional heating, fluid pressure, and the resistance to fault motion. *J Geophys Res*, *85*(B11), 6097–6112. https://doi.org/10.1029/JB085iB11p06097

Merriman, R.J. (1987). Low Temperature Metamorphism. *Clay Minerals,* 22(4), 486-487. https://doi.org/10.1180/claymin.1987.022.4.13

Moore, D. E., & Rymer, M. J. (2007). Talc-bearing serpentinite and the creeping section of the San Andreas fault. *Nature*, *448*(7155), 795–797. https://doi.org/10.1038/nature06064

O'Hara, K. (2004). Paleo-stress estimates on ancient seismogenic faults based on frictional heating of coal. *Geophys Res Lett*, *31*(3), L03601. https://doi.org/10.1029/2003GL018890

Ramseyer, K., Boles, J. R., & Lichtner, P. C. (1992). Mechanism of plagioclase albitization. *Journal of Sedimentary Research*, *62*(3), doi:10.1306/D42678FC-2B26-11d7-8648000102C1865D

Rice, J. R. (2006), Heating and weakening of faults during earthquake slip, *J. Geophys. Res.*, 111, B05311, doi:10.1029/2005JB004006.

Sakaguchi, A. (2011). Sakaguchi et al. Vitrinite Reflectance Methods Appendix. *GSA Data Repository*, 1–1. Retrieved from ftp://rock.geosociety.org/pub/reposit/2011/2011126.pdf

Sakaguchi, A., Chester, F., Curewitz, D., Fabbri, O., Goldsby, D., Kimura, G., et al. (2011). Seismic slip propagation to the updip end of plate boundary subduction interface faults: Vitrinite reflectance geothermometry on Integrated Ocean Drilling Program NanTro SEIZE cores. *Geology*, *39*(4), 395–398. https://doi.org/10.1130/G31642.1

Sammis, C. G., Osborne, R. H., Anderson, J. L., Banerdt, M., & White, P. (1986). Self-similar cataclasis in the formation of fault gouge. *Pure and Applied Geophysics PAGEOPH*, *124*(1-2), 53–78. https://doi.org/10.1007/BF00875719

Sammis, C., King, G., & Biegel, R. (1987). The kinematics of gouge deformation. *Pure and Applied Geophysics PAGEOPH*, *125*(5), 777–812. https://doi.org/10.1007/BF00878033

Schleicher, A. M., Tourscher, S. N., van der Pluijm, B. A., & Warr, L. N. (2009). Constraints on mineralization, fluid-rock interaction, and mass transfer during faulting at 2–3 km depth from the SAFOD drill hole. *J Geophys Res*, *114*(B4), B04202, doi: 10.1029/2008JB006092

Schleicher, A. M., van der Pluijm, B. A., & Warr, L. N. (2010). Nanocoatings of clay and creep of the San Andreas fault at Parkfield, California. *Geology*, *38*(7), 667–670. https://doi.org/10.1130/G31091.1

Schleicher, A. M., van der Pluijm, B. A., Solum, J. G., & Warr, L. N. (2006). Origin and significance of clay-coated fractures in mudrock fragments of the SAFOD borehole

(Parkfield, California). *Geophys Res Lett*, *33*(16), L16313. https://doi.org/10.1029/2006GL026505

Schleicher, A., Warr, L., & van der Pluijm, B. (2009). On the origin of mixed-layered clay minerals from the San Andreas Fault at 2.5–3 km vertical depth (SAFOD drillhole at Parkfield, California). *Contributions to Mineralogy and Petrology*, *157*(2), 173–187. https://doi.org/10.1007/s00410-008-0328-7

Schulz, S. S. & Wallace, R. E. (2016). The San Andreas Fault, The U.S. Geological Survey, URL: https://pubs.usgs.gov/gip/earthq3/

Sibson, R. H. (2003). Thickness of the Seismic Slip Zone. *Bulletin of the Seismological Society of America*, *93*(3), 1169–1178. https://doi.org/10.1785/0120020061

Sibson, R. H. (1975). Generation of Pseudotachylyte by Ancient Seismic Faulting. *Geophysical Journal International*. https://doi.org/10.1111/j.1365-246X.1975.tb06195.x

Solum, J. G., Hickman, S. H., Lockner, D. A., Moore, D. E., van der Pluijm, B. A., Schleicher, A. M., & Evans, J. P. (2006). Mineralogical characterization of protolith and fault rocks from the SAFOD Main Hole. *Geophys Res Lett*, *33*(21), L21314. https://doi.org/10.1029/2006GL027285

Spray, J. G. (1997). Superfaults. *Geology*, *25*(7), 579–582. https://doi.org/10.1130/0091-7613(1997)025<0579:S>2.3.CO;2

Springer, S. D., Evans, J. P., Garver, J. I., Kirschner, D., & Janecke, S. U. (2009). Arkosic rocks from the San Andreas Fault Observatory at Depth (SAFOD) borehole, central California: Implications for the structure and tectonics of the San Andreas fault zone. *Lithosphere*, *1*(4), 206–226. https://doi.org/10.1130/L13.1

Sweeney, J. J., & Burnham, A. K. (1990). Evaluation of a Simple Model of Vitrinite Reflectance Based on Chemical Kinetics (1). *AAPG Bulletin*, *74*(10), 1559–1570.

Taylor, G. H., Teichmüller, M., Davis, A., & Diessel, C. (1998). Organic petrology. Gebrüder Borntraeger.

Tembe, S., Lockner, D. A., Solum, J. G., Morrow, C. A., Wong, T., & Moore, D. E. (2006). Frictional strength of cuttings and core from SAFOD drillhole phases 1 and 2. *Geophys Res Lett*, *33*, L23307. https://doi.org/10.1029/2006GL027626

Tembe, S., Lockner, D., & Wong, T.-F. (2009). Constraints on the stress state of the San Andreas Fault with analysis based on core and cuttings from San Andreas Fault Observatory at Depth (SAFOD) drilling phases 1 and 2. *Journal of Geophysical*

Research: Solid Earth (1978–2012), *114*(B11). https://doi.org/10.1029/2008JB005883

Tullis, T.E. (2015). Mechanisms for Friction of Rock at Earthquake Slip Rates, Ch. 6 in Earthquake Seismology, Vol. 4 of Treatise on Geophysics, Second Edition, edited by H. Kanamori, Gerald Schubert (editor-in-chief), Elsevier, Oxford, UK, p. 139-159, doi:10.1016/B978-0-444-53802-4.00073-7.

Vrolijk, P., & van der Pluijm, B. A. (1999). Clay gouge. *Journal of Structural Geology*, *21*(8-9), 1039–1048. https://doi.org/10.1016/S0191-8141(99)00103-0

Wibberley, C. A. J., & Shimamoto, T. (2003). Internal structure and permeability of major strike-slip fault zones: the Median Tectonic Line in Mie Prefecture, Southwest Japan. *Journal of Structural Geology*, *25*(1), 59–78. https://doi.org/10.1016/S0191-8141(02)00014-7

Williams, C. F. (2004). Heat flow in the SAFOD pilot hole and implications for the strength of the San Andreas Fault. *Geophys Res Lett*, *31*(15), L15S14–. https://doi.org/10.1029/2003GL019352

Zoback, M.D., Hickman, S., and Ellsworth, W.L. (2010). Scientific drilling into the San Andreas Fault. *Eos, Trans. AGU*, 91(22):197–204, doi:10.1029/2010EO220001.

Zoback, M. D., S. Hickman, W. Ellsworth, and the SAFOD Science Team: Scientific drilling into the San Andreas Fault Zone—An overview of SAFOD's first five years, *Scientific Drilling* 11, 14-28, doi:10.2204/iodp.sd.11.02.2011, 2011.